sensors

MDPI

Article

A Linear Rehabilitative Motion Planning Method with a Multi-Posture Lower-Limb Rehabilitation Robot

Xincheng Wang [1,2], Musong Lin [3], Lingfeng Sang [4], Hongbo Wang [1,2,5], Yongfei Feng [6], Jianye Niu [1,2], Hongfei Yu [7,8,*] and Bo Cheng [9,*]

1 Hebei Provincial Key Laboratory of Parallel Robot and Mechatronic System, Yanshan University, Qinhuangdao 066000, China; wangxincheng@stumail.ysu.edu.cn (X.W.); hongbo_w@ysu.edu.cn (H.W.); jyniu@ysu.edu.cn (J.N.)
2 School of Mechanical Engineering, Yanshan University, Qinhuangdao 066000, China
3 Department of Environmental Engineering, Hebei University of Environmental Engineering, Qinhuangdao 066000, China; linmusong@hebuee.edu.cn
4 Ningbo Key Laboratory of Aging Health Equipment and Service Technology, Ningbo Polytechnic, Ningbo 315211, China; sanglingfeng@163.com
5 Academy for Engineering & Technology, Fudan University, Shanghai 200000, China
6 Faculty of Mechanical Engineering & Mechanics, Ningbo University, Ningbo 315211, China; fengyongfei@nbu.edu.cn
7 Collaborative Innovation Center for Port Industry Development in Coastal Areas, Qinhuangdao 066000, China
8 Hebei Technology Innovation Center for Intelligent Industrial Design, Qinhuangdao 066000, China
9 Qinhuangdao Hospital of Traditional Chinese Medicine, Qinhuangdao 066000, China
* Correspondence: yhf0335@ysu.edu.cn (H.Y.); barrycb@163.com (B.C.)

Abstract: In rehabilitation, physicians plan lower-limb exercises via linear guidance. Ensuring efficacy and safety, they design patient-specific paths, carefully plotting smooth trajectories to minimize jerks. Replicating their precision in robotics is a major challenge. This study introduces a linear rehabilitation motion planning method designed for physicians to use a multi-posture lower-limb rehabilitation robot, encompassing both path and trajectory planning. By subdividing the lower limb's action space into four distinct training sections and classifying this space, we articulate the correlation between linear trajectories and key joint rehabilitation metrics. Building upon this foundation, a rehabilitative path generation system is developed, anchored in joint rehabilitation indicators. Subsequently, high-order polynomial curves are employed to mimic the smooth continuity of traditional rehabilitation trajectories and joint motions. Furthermore, trajectory planning is refined through the resolution of a constrained quadratic optimization problem, aiming to minimize the abrupt jerks in the trajectory. The optimized trajectories derived from our experiments are compared with randomly generated trajectories, demonstrating the suitability of trajectory optimization for real-time rehabilitation trajectory planning. Additionally, we compare trajectories generated based on the two groups of joint rehabilitation indicators, indicating that the proposed path generation system effectively assists clinicians in executing efficient and precise robot-assisted rehabilitation path planning.

Keywords: rehabilitative motion planning; multi-posture lower-limb rehabilitation robot; joint rehabilitation; high-order polynomial curves; minimized jerk

check for updates

Citation: Wang, X.; Lin, M.; Sang, L.; Wang, H.; Feng, Y.; Niu, J.; Yu, H.; Cheng, B. A Linear Rehabilitative Motion Planning Method with a Multi-Posture Lower-Limb Rehabilitation Robot. *Sensors* **2024**, *24*, 7506. https://doi.org/10.3390/s24237506

Academic Editors: Paolo Mercorelli and Giovanni Saggio

Received: 15 September 2024
Revised: 18 November 2024
Accepted: 22 November 2024
Published: 25 November 2024

Copyright: © 2024 by the authors. Licensee MDPI, Basel, Switzerland. This article is an open access article distributed under the terms and conditions of the Creative Commons Attribution (CC BY) license (https://creativecommons.org/licenses/by/4.0/).

1. Introduction

It is important to restore balance and walking ability for lower-limb rehabilitation in stroke. Li et al. [1–3] proposed that stroke leads to a decrease in knee joint flexion on the paralyzed side, and the knee flexion should be considered in therapy. Rybar et al. [4–6] emphasized the importance of hip flexors for standing and walking. The enhancement of lower-limb joint flexion ability helps to improve walking ability and gait

speed in hemiplegic patients [7,8]. In addition, Schindler-Ivens et al. [9] pointed out that stroke patients have more passive joint extension, and additional joint extension exercise is unlikely to improve their motor ability. Pollock et al. [10] pointed out that training the affected lower limb in a rapid flexion mode may improve the walking and balance ability. Gomez-Cuaresma et al. [11] suggested that prolonged passive stretching of the entire motion range may help improve spasticity. In short, the ultimate joint flexion angle, the ultimate joint flexion frequency, and the ultimate joint motion range are important indicators of rehabilitation. Therefore, this paper explores the relationship between the linear trajectories and the corresponding joint rehabilitation characteristics of the indicators.

The passive training of linear trajectory is mainly achieved by physicians dragging the patient's impaired limb or through the assistance of the rehabilitation robot. In traditional therapy, physicians can plan the optimal trajectories by touch and experience. However, when using the robot, physicians cannot learn the joints' rehabilitation characteristics corresponding to the preset trajectory, making it difficult to plan the optimal trajectory. Typical multi-DOF lower-limb rehabilitation robots usually complete fixed trajectories through a single driving mechanism. The Lambda [12], the symmetrical lower-limb rehabilitation robot [13], and the CPM/CAM physiotherapy device [14] can complete circular trajectories. Horizontal lower limbs rehabilitation robot [15] and Fisiotek [16] can complete the horizontal linear trajectory. Due to their simple structure and low cost, these types of robots usually use a relatively simple trajectory planning method. Sitting and lying exoskeleton lower-limb rehabilitation robot is applicable to patients in multiple rehabilitation stages. The Motion Maker [17,18] can automatically guide patients to perform passive flexion training on the hip, knee, and ankle joints along a pre-selected trajectory. Other typical sitting and lying rehabilitation robots include Physiotherabot [19], TEMLX2 typeD [20], and NeXOS [21]. The sitting–lying lower-limb rehabilitation robot [22] provides a teaching training function for physicians, allowing them to plan personalized trajectories through the touch screen. Wearable exoskeleton robots and suspended rehabilitation robots are mainly used for gait rehabilitation, which are mainly composed of two symmetrical mechanical legs. Rewalk [23,24] can simulate the normal gait of the human body at an appropriate speed based on a preset motion model. Other typical wearable exoskeleton robots include HAL [25,26], Exo-H2 [27,28], and KineAssist [29]. Lokomat [30–32] is a suspended rehabilitation robot with a weight reduction suspension system. It guides motion based on preset gait motion patterns. Other typical suspended rehabilitation robots include LOPES [33] and ALEX [34]. The above gait rehabilitation robots either use predefined gait trajectories or use the mapping of healthy limbs to plan the trajectory. In addition, Guo et al. [35,36] designed a wearable teaching device for physicians to provide personalized gait trajectories for patients.

The above lower-limb rehabilitation robots have provided various trajectory planning methods for physicians. However, the preset gait trajectory is based on the trajectory of the function limb, which is not suitable for the sitting and lying robot [37]. The mapping of the function limb to the impaired limb requires auxiliary wearable equipment or structure with both legs, unfitting for robots with a single leg. The teaching device worn on the physician's leg may result in a mismatch of joint mobility, leading to the trajectory exceeding a safe range. Moreover, it requires physicians relatively more labor and time. The preset or custom trajectory through the screen is common and easy to implement, but it is difficult for physicians to select or draw the optimal trajectory based on the rehabilitation needs of joints.

On the other hand, the previously reported works mostly focused on offline programming tasks [38,39]. With the increasing demands for rehabilitation, an increasing number of practical tasks require the rapid planning of movements for real-time execution. Therefore, real-time trajectory planning for rehabilitation robots has consistently been an important issue for generating safe and efficient trajectories. Real-time trajectory planning has been well applied in the field of autonomous driving. However, in dynamic environments, real-time trajectory planning based on optimization that is specifically tailored to the joint

rehabilitation needs of rehabilitation robots is rarely found in the literature. The reported real-time trajectory planning in the references is limited to path generation and does not address the performance of the robot and the rehabilitation.

A multistage hemiplegic lower-limb rehabilitation robot (MHLRR) [40] was designed by our team to conduct motor rehabilitation of lower limbs for patients with hemiplegia in multiple recovery stages. It has several features, including multistage usability, bi-side usability, lightweight design, mechanically adjustable limits, and easy mobility. Based on the lower-limb rehabilitation robot, this paper will deal with the foregoing problem, which is structured as follows:

- Step 1: Patient-specific lower-limb parameters are input into the system, leading to the creation of a personalized lower-limb motion space. This space is subsequently segmented into distinct training regions, categorized according to the classification criteria established for the space. Building upon this classification, the initial and final positions, as well as intermediate via points, are meticulously defined. These points are strategically positioned within the valid training region of the action space, aligning with the five joint rehabilitation indicator parameters that have been set by a physician based on their clinical experience.
- Step 2: Utilizing the defined key points, a parametric path is constructed via a seventh-degree polynomial curve. The coefficients of this polynomial are then fine-tuned through optimization to accurately represent the intended rehabilitation trajectory. The robot's end effector is designed to minimize jerk, replicating a gentle and low-impact rehabilitative trajectory. This mimics the approach traditionally employed by physicians, who guide the affected limbs along such trajectories during therapy.
- Step 3: The kinematic curve of the rehabilitation trajectory is converted into joint space through inverse kinematics. The joint movements are then transmitted to the controller, which drives the lower-limb rehabilitation robot's end effector to track the generated trajectory.

The remainder of this paper is organized as follows. Section 2 introduces the multi-posture lower-limb rehabilitation robot. Section 3 presents the rehabilitative path planning based on the joint rehabilitation indicators. In Section 4, the rehabilitative trajectory planning-based jerk minimization is illustrated with the two experimental rehabilitative trajectories to verify the effectiveness. Finally, the conclusions are drawn.

2. Multi-Posture Lower-Limb Rehabilitation Robot

2.1. Mechanism

As shown in Figure 1, the primary design considerations are the adaptability of rehabilitation in multiple recovery stages and the adjustability on the bilateral training side. For multistage rehabilitation based on Brunnstrom's theory, the MHLRR's training posture must be versatile enough to support patients in lying, sitting, and standing positions, aligning with their stages of recovery. Furthermore, the robot's training apparatus should be configurable to address the specific hemiplegic side, ensuring personalized therapy. To this end, it is vital that the ranges of joint motion and the height of leg orthosis can be adjusted according to the recovery stage and the affected side.

Based on the modular design concept, the MHLRR mainly consists of four parts, including the balance mechanism, the hip joint mechanism, the knee joint mechanism, and the ankle joint mechanism, as depicted in Figure 2. This design philosophy ensures that the leg orthosis can be adjusted in height from 540 mm to 1040 mm, providing a versatile range that spans from the hip joint axis to the ground level. This adaptability is achieved through the manipulation of the lifting columns, catering to the diverse needs of patients across various stages of recovery and enabling rehabilitation in lying, sitting, or standing positions. This is achieved by actuating the hip joint motor, which symmetrically aligns the leg orthosis with respect to the coronal plane, thus allowing for bilateral training adaptability.

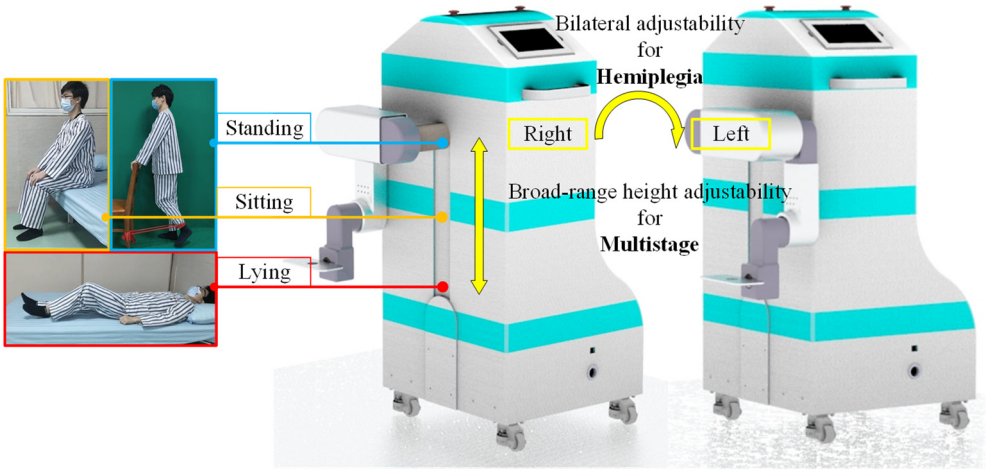

Figure 1. Prototype of the MHLRR. MHLRR: Multistage Hemiplegic Lower-Limb Rehabilitation Robot. Multiple training postures for patients in all stages of recovery. Multiple training sides for patients with hemiplegia.

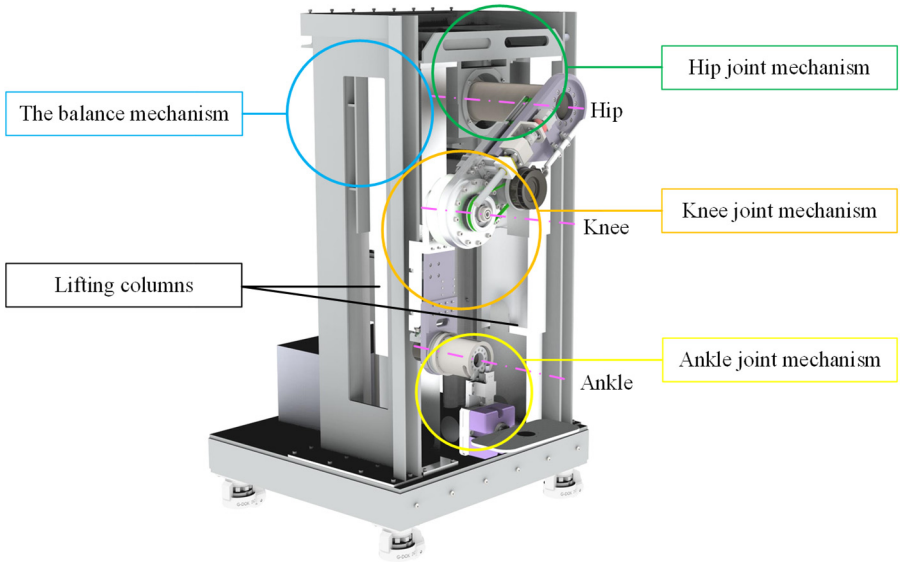

Figure 2. Overall structure of the MHLRR.

2.2. Description of the Action Space

According to the physiological structure of the human lower limb, the rehabilitation robot is simplified to a link structure, as shown in Figure 3. The dimensions of the thigh and calf are denoted as l1 and l2, respectively. The kinematic model is depicted in Figure 3. The symbols O, A, and B correspond to the hip joint, knee joint, and ankle joint, respectively. The rotation angles of the hip and knee joints are denoted by α and β, respectively. The hip joint's center, point O, is established as the coordinate system's origin, with the ankle joint B designated as the terminal point. Subsequently, the relationship between the coordinates of point B and the joint angles can be derived using forward and inverse kinematics as follows:

$$\begin{cases} x_B = l_1 \cdot \cos\alpha + l_2 \cdot \cos(\alpha+\beta) \\ y_B = l_1 \cdot \sin\alpha + l_2 \cdot \sin(\alpha+\beta) \\ \alpha = \arctan\frac{y_B}{x_B} + \arccos\frac{{l_1}^2-{l_2}^2+{x_B}^2+{y_B}^2}{2\cdot l_1\cdot\sqrt{{x_B}^2+{y_B}^2}} \\ \beta = \arccos\frac{{x_B}^2+{y_B}^2-{l_1}^2-{l_2}^2}{2\cdot l_1\cdot l_2} \end{cases} \quad (1)$$

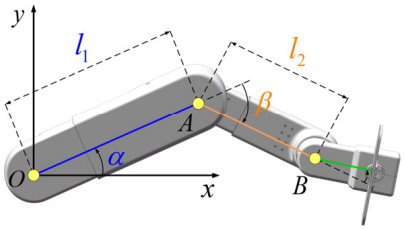

Figure 3. The kinematic model.

The workspace of the proposed robot is adjustable according to the different action spaces of patients. It is determined by four factors, including the affected side, the training posture, the joint motion range, and the lower-limb length. Figure 4 shows the definition of the action space of a common patient in a sitting position.

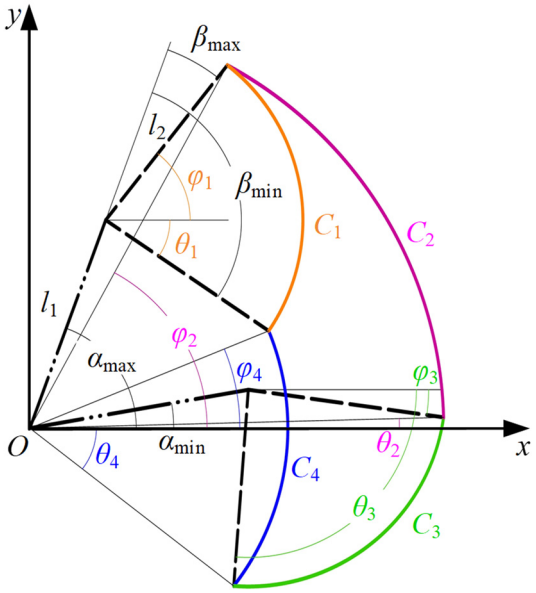

Figure 4. Definition and nomenclature of the action space. This figure represents a sitting position, with the patient's joint ranges of motion set to $\alpha_{max} = 75°$, $\alpha_{min} = 10°$, $\beta_{max} = -5°$, and $\beta_{min} = -95°$.

Point O signifies the hip joint, while l_1 and l_2 denote the lengths of the thigh and calf, respectively. The terms α_{min} and α_{max} correspond to the minimum and maximum flexion angles of the hip joint, respectively, while β_{min} and β_{max} denote the minimum and maximum extension angles of the knee joint. In our coordinate system, counterclockwise rotation is designated as the positive direction. The hip angle is conventionally set to zero in both sitting and lying positions when the thigh is aligned parallel to the horizontal axis. In parallel, the knee angle is also defined as zero when the calf is in direct alignment with the thigh, irrespective of the patient's position. This standardized approach ensures consistency and clarity in the measurement and analysis of joint angles throughout the rehabilitation process. Curve C_1 delineates the path of the end point as the knee joint moves from its minimum to maximum angle with the hip joint fixed at its maximum angle. Similarly, the three other curves, C_2, C_3, and C_4, can be obtained. To enhance the clarity of these four workspace curves, we introduce Equation (2) for a more comprehensive depiction, which is expressed as

$$Ci = (x_i, y_i, r_i, \theta_i, \varphi_i)(i = 1, 2, 3, 4), \tag{2}$$

where θ_i, φ_i, (x_i, y_i), and r_i represent the start angle, the end angle, the center coordinates, and the radius of the curve C_i, respectively. Then, the expressions for each parameter can be obtained as

$$\begin{cases} r_1 = l_2; r_2 = \sqrt{{l_1}^2 + {l_2}^2 + 2 \cdot l_1 \cdot l_2 \cdot \cos \beta \max} \\ r_3 = l_2; r_4 = \sqrt{{l_1}^2 + {l_2}^2 + 2 \cdot l_1 \cdot l_2 \cdot \cos \beta \min} \\ (x_1, y_1) = (l_1 \cdot \cos \alpha \max, l_1 \cdot \sin \alpha \max); (x_2, y_2) = (0, 0) \\ (x_3, y_3) = (l_1 \cdot \cos \alpha \min, l_1 \cdot \sin \alpha \min); (x_4, y_4) = (0, 0) \\ \theta_1 = \alpha \max + \beta \min; \theta_2 = \alpha \min - \arccos \frac{l_1 + l_2 \cdot \cos \beta \max}{\sqrt{{l_1}^2 + {l_2}^2 + 2 \cdot l_1 \cdot l_2 \cdot \cos \beta \max}} \\ \theta_3 = \alpha \min + \beta \min; \theta_4 = \alpha \min - \arccos \frac{l_1 + l_2 \cdot \cos \beta \min}{\sqrt{{l_1}^2 + {l_2}^2 + 2 \cdot l_1 \cdot l_2 \cdot \cos \beta \min}} \\ \varphi_1 = \alpha \max + \beta \max; \varphi_2 = \alpha \max - \arccos \frac{l_1 + l_2 \cdot \cos \beta \max}{\sqrt{{l_1}^2 + {l_2}^2 + 2 \cdot l_1 \cdot l_2 \cdot \cos \beta \max}} \\ \varphi_3 = \alpha \min + \beta \max; \varphi_4 = \alpha \max - \arccos \frac{l_1 + l_2 \cdot \cos \beta \min}{\sqrt{{l_1}^2 + {l_2}^2 + 2 \cdot l_1 \cdot l_2 \cdot \cos \beta \min}} \end{cases} . \quad (3)$$

It serves as the theoretical foundation for calculating the coordinates of the starting and ending points of the linear trajectory when it is at different positions within the action space.

The maximum joint ranges of motion of MHLRR under lying, sitting, and standing postures are shown in Table 1.

Table 1. The maximum joint ranges of motion of MHLRR under different postures.

Joint/Posture	Lying	Sitting	Standing
Hip	0°~130°	0°~80°	−20°~60°
Knee	−135°~0°	−135°~0°	−135°~0°
Ankle	−45°~30°	−45°~30°	−45°~30°

3. Rehabilitative Path Planning Based on Joint Rehabilitation Indicators

3.1. The Division of Training Section and the Classification of the Action Space

The CPM (Continuous Passive Motion) linear trajectory training is a widely adopted rehabilitation technique, typically implemented by clinicians who manually guide the patient's lower limb through a reciprocating linear motion. This method is particularly beneficial during the early recovery stages for patients experiencing muscle paralysis or diminished muscle strength, as it facilitates passive training that preserves the joint's large range of motion, thereby preventing joint contractures and deformities. As patients progress into the middle and late stages of recovery, where they may have regained some muscle strength but still lack the ability to achieve full joint flexion, a more targeted approach becomes necessary. This involves focusing on maximum flexion training to further enhance joint mobility.

Building on these principles, this study delves into the joint rehabilitation characteristics of the CPM linear trajectory in both lying and sitting positions. The analysis aims to tailor the rehabilitation process to patients with diverse action spaces and varying joint rehabilitation requirements, ensuring a more personalized and effective treatment plan.

To effectively encapsulate the joint rehabilitation characteristics of the horizontal linear trajectory ensemble within the dynamic action space, it is imperative to quantify the distinct types of lower-limb action spaces. The variables P_{ij} (i = 1, 3; j = 2, 4) are designated as the intersection points between arcs C_i and C_j. Points M and N represent the initiation and termination points, respectively, of the intersection between the horizontal linear trajectory and the action space. Points Q_1 and Q_2 are identified as the upper tangent points of the circle encompassing arcs C_1 and C_2, while Q_3 and Q_4 correspond to the lower tangent

points of the circle for arcs C_3 and C_4. The coordinates of these eight pivotal points can be ascertained through kinematic analysis as follows:

$$\begin{cases} P_{12}(l_1 \cdot \cos\alpha_{max} + l_2 \cdot \cos(\alpha_{max} + \beta_{max}), l_1 \cdot \sin\alpha_{max} + l_2 \cdot \sin(\alpha_{max} + \beta_{max})) \\ P_{14}(l_1 \cdot \cos\alpha_{max} + l_2 \cdot \cos(\alpha_{max} + \beta_{min}), l_1 \cdot \sin\alpha_{max} + l_2 \cdot \sin(\alpha_{max} + \beta_{min})) \\ P_{23}(l_1 \cdot \cos\alpha_{min} + l_2 \cdot \cos(\alpha_{min} + \beta_{max}), l_1 \cdot \sin\alpha_{min} + l_2 \cdot \sin(\alpha_{min} + \beta_{max})) \\ P_{34}(l_1 \cdot \cos\alpha_{min} + l_2 \cdot \cos(\alpha_{min} + \beta_{min}), l_1 \cdot \sin\alpha_{min} + l_2 \cdot \sin(\alpha_{min} + \beta_{min})) \\ Q_1(l_1 \cdot \cos\alpha_{max}, l_1 \cdot \sin\alpha_{max} + l_2); Q_2(0, \sqrt{{l_1}^2 + {l_2}^2 + 2 \cdot l_1 \cdot l_2 \cdot \cos\beta_{max}}) \\ Q_3(l_1 \cdot \cos\alpha_{min}, l_1 \cdot \sin\alpha_{min} - l_2); Q_4(0, -\sqrt{{l_1}^2 + {l_2}^2 + 2 \cdot l_1 \cdot l_2 \cdot \cos\beta_{min}}) \end{cases} . \quad (4)$$

The action space is segmented into multiple training sections by horizontal lines intersecting at these key points. The principles for section division are as follows: within the same section, all starting points of linear trajectories are on the same arc C_i. Moreover, all ending points are also on the same arc C_j. Across different sections, there exists at least one pair of trajectories whose starting or ending points do not align on the same arc. Additionally, sections composed of identical arcs C_iC_j (where $i = j$) are designated as section 0, while those composed of distinct arcs C_iC_j (where $i \neq j$) are sequentially labeled as sections 1 to 3 from the bottom upward.

Each training section is demarcated by boundary lines intersecting at key points and a pair of arcs, as illustrated in Figure 5. Points P_{12}, Q_1, and Q_2 are situated above P_{14} and P_{23}, whereas points P_{34}, Q_3, and Q_4 are positioned below P_{14} and P_{23}, according to the graphical method. Consequently, the action space is stratified into three distinct regions: the bottom, the middle, and the top.

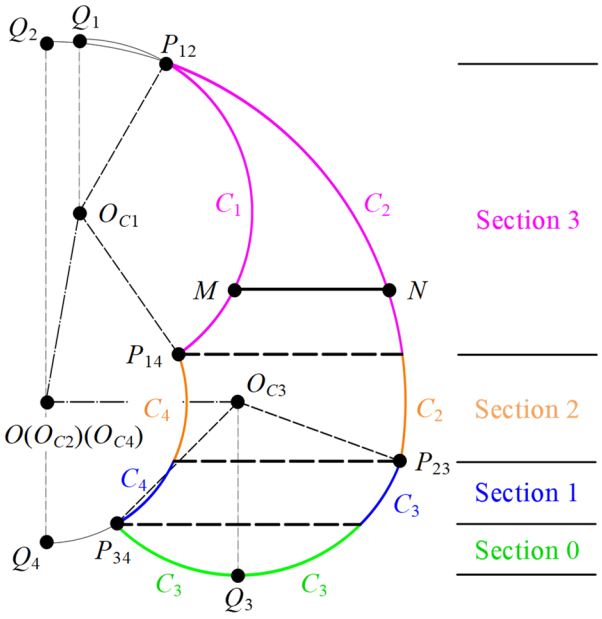

Figure 5. Section division of the action space.

The classification method of the action space is proposed by analyzing the distribution of key points across the bottom, middle, and top regions. Firstly, we focus on the positioning of points P_{34}, Q_3, and Q_4 within the bottom region of the action space. The scenarios for one situation in the lying position and two in the sitting position are depicted in Figure 5. It is crucial to recognize that in stroke patients with lower-limb impairments, the hip joint's free extension is typically unimpaired, whereas achieving a significant flexion angle is more challenging. Consequently, the minimum flexion angles for the hip joint in the lying and sitting positions are established at $\alpha_{min} = 50°$ and $\alpha_{min} = 0°$, respectively.

Utilizing Equation (4), it becomes evident that the positions of the three points P_{34}, Q_3, and Q_4 are interrelated with α_{min}, β_{min}, l_1, and l_2. In the lying position, there is a singular scenario where $x_{Q4} < x_{Q3} < x_{P34}$, given the conditions $\alpha_{min} = 50°$, $-135° \leq \beta_{min} < 0°$ and Equation (5). This leads to the conclusion that in the lying position, there is a single configuration at the bottom of the action space: when $-135° \leq \beta_{min} < 0°$, P_{34} is the lowest point, and both Q_3 and Q_4 lie outside the action space, as shown in Figure 6a.

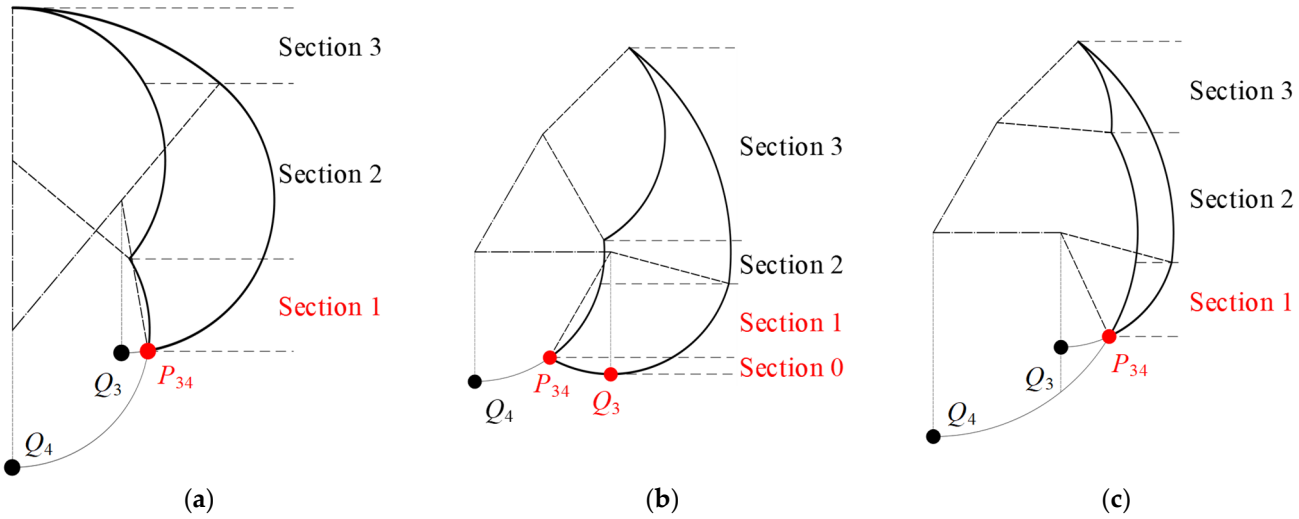

Figure 6. The positioning of points P34, Q3, and Q4 within the bottom region of the action space: (**a**) $x_{Q4} < x_{Q3} < x_{P34}$ in lying position; (**b**) $x_{Q4} < x_{P34} < x_{Q3}$ in sitting position; (**c**) $x_{Q4} < x_{Q3} \leq x_{P34}$ in sitting position.

In the sitting position, the condition $x_{Q4} < x_{P34}$ can be deduced from $\alpha_{min} = 0°$, $-135° \leq \beta_{min} < 0°$, and $l_1 > l_2$. Subsequently, based on Equation (4), it can be obtained that $-135° \leq \beta_{min} < -90°$ when $x_{Q4} < x_{P34} < x_{Q3}$, and $-90° \leq \beta_{min} \leq 0°$ when $x_{Q4} < x_{Q3} \leq x_{P34}$. Therefore, it can be concluded that in the sitting position, there are two distinct scenarios at the bottom of the action space. When $-135° \leq \beta_{min} < -90°$, P_{34} serves as the critical boundary point, Q_3 is the lowest and critical boundary point, and Q_4 is outside the action space, as shown in Figure 6b. Conversely, when $-90° \leq \beta_{min} \leq 0°$, P_{34} is both the lowest and critical boundary point, with Q_3 and Q_4 situated outside the action space, as shown in Figure 6c.

Secondly, we analyze the positioning of points P_{14} and P_{23} within the middle region of the action space, which encompasses six distinct scenarios: $y_{P14} > y_{P23}$, $y_{P14} < y_{P23}$, and $y_{P14} = y_{P23}$ in lying and sitting positions. According to Equation (4), the positional relationship between these two points is influenced by all the parameters involved. By solving for the conditions that satisfy each of these scenarios, we can determine their relative positions, as illustrated in Figure 7.

Consequently, we can deduce the following conclusions: Point P_{14} is situated above P_{23} when the inequality $l_1 \cdot \sin\alpha_{max} - l_1 \cdot \sin\alpha_{min} + l_2 \cdot \sin(\alpha_{max} + \beta_{min}) - l_2 \cdot \sin(\alpha_{min} + \beta_{max}) > 0$ holds true. Conversely, P_{14} is located below P_{23} when the inequality $l_1 \cdot \sin\alpha_{max} - l_1 \cdot \sin\alpha_{min} + l_2 \cdot \sin(\alpha_{max} + \beta_{min}) - l_2 \cdot \sin(\alpha_{min} + \beta_{max}) < 0$ is met. Lastly, points P_{14} and P_{23} are aligned at the same height when the equation $l_1 \cdot \sin\alpha_{max} - l_1 \cdot \sin\alpha_{min} + l_2 \cdot \sin(\alpha_{max} + \beta_{min}) - l_2 \cdot \sin(\alpha_{min} + \beta_{max}) = 0$ is satisfied.

Thirdly, proceeding to the analysis of points P_{12}, Q_1, and Q_2 in the top region of the action space, we observe three distinct scenarios in the lying position and a single scenario in the sitting position, as depicted in Figure 8. It is important to note that patients with stroke-induced lower-limb disorders often have limited knee joint flexion, while the knee's free extension is typically preserved. Hence, the knee joint's maximum angle range in both lying and sitting positions is confined to $-90° < \beta_{max} \leq 0°$.

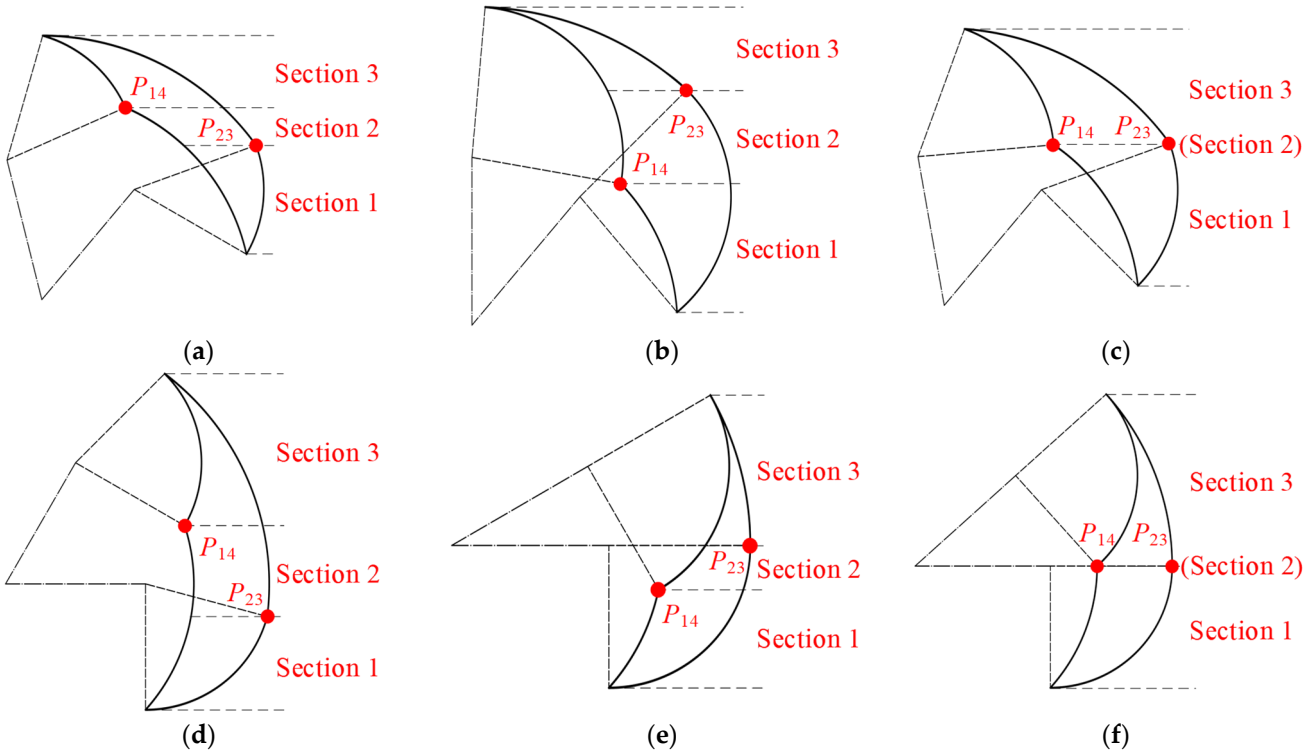

Figure 7. The positioning of points P_{14} and P_{23} within the middle region of the action space: (**a**) $y_{P14} > y_{P23}$ in lying position; (**b**) $y_{P14} < y_{P23}$ in lying position; (**c**) $y_{P14} = y_{P23}$ in lying position; (**d**) $y_{P14} > y_{P23}$ in sitting position; (**e**) $y_{P14} < y_{P23}$ in sitting position; (**f**) $y_{P14} = y_{P23}$ in sitting position.

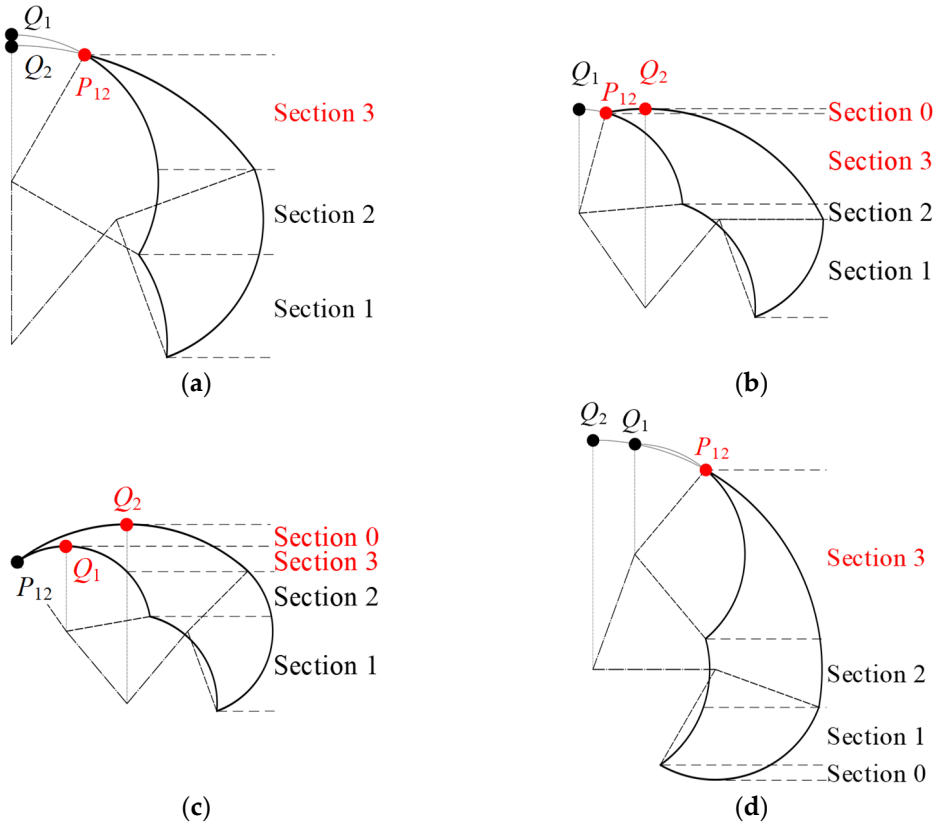

Figure 8. The positioning of points P_{12}, Q_1, and Q_2 within the top region of the action space: (**a**) $x_{Q1} \leq x_{P12}$ and $x_{Q2} \leq x_{P12}$ in a lying position; (**b**) $x_{Q1} \leq x_{P12} < x_{Q2}$ in a lying position; (**c**) $x_{P12} < x_{Q1} < x_{Q2}$ in a lying position; (**d**) $x_{Q2} < x_{Q1} < x_{P12}$ in sitting position.

Equation (5) reveals that the positions of these three points are interdependent on α_{max}, β_{max}, l_1, and l_2. In the lying position, we first examine the relationship between x_{Q1} and x_{Q2}. When $x_{Q1} \geq x_{Q2}$, there is a singular scenario where $x_{Q2} \leq x_{Q1} \leq x_{P12}$, which corresponds to the condition $50° < \alpha_{max} \leq 90°$. When $x_{Q1} < x_{Q2}$, three possible situations arise: $x_{Q1} < x_{Q2} \leq x_{P12}$, $x_{Q1} \leq x_{P12} < x_{Q2}$, and $x_{P12} < x_{Q1} < x_{Q2}$, each with specific conditions that can be solved. Thus, in the lying position, there are three possible configurations at the top of the action space. For $50° < \alpha_{max} \leq 90°$, or when $90° < \alpha_{max} \leq 130°$ and $\beta_{max} \geq 180° - \alpha_{max} - \arccos(\cos\alpha_{max} \cdot l_1/l_2)$, there exists $x_{Q1} \leq x_{P12}$ and $x_{Q2} \leq x_{P12}$. Here, P_{12} is the highest and critical boundary point, with both Q_1 and Q_2 either outside or coinciding with the action space. For $90° < \alpha_{max} \leq 130°$, $\beta_{max} < 180° - \alpha_{max} - \arccos(\cos\alpha_{max} \cdot l_1/l_2)$, and $-\alpha_{max} + 90° \leq \beta_{max} \leq -\alpha_{max} + 130°$, there exists $x_{Q1} \leq x_{P12} < x_{Q2}$. In this case, Q_2 is the highest and critical boundary point, P_{12} is a critical boundary point, and Q_1 is outside the action space. When $90° < \alpha_{max} \leq 130°$, $\beta_{max} < 180° - \alpha_{max} - \arccos(\cos\alpha_{max} \cdot l_1/l_2)$, and $-\alpha_{max} + 90° \leq \beta_{max} \leq -\alpha_{max} + 130°$, there exists $x_{P12} < x_{Q1} < x_{Q2}$. Here, Q_2 is the highest and critical boundary point, Q_1 is a critical boundary point, and P_{12} is merely a common boundary point.

In the sitting position, given the conditions $0° < \alpha_{max} \leq 80°$ and $-90° < \beta_{max} \leq 0°$, it is determined that $x_{Q2} < x_{Q1} < x_{P12}$. Therefore, there is one singular scenario at the top of the action space in the sitting position, where P_{12} is the highest and critical boundary point, and both Q_1 and Q_2 are situated outside the action space.

Following the comprehensive analysis of the key boundary points across the bottom, middle, and top regions, we can conclude that there are nine situations in a lying position and six situations in a sitting position. Building on this foundation, a classification method for the action space is devised, where the action spaces with the same section number and one-to-one correspondence of key boundary points are considered of the same type.

There are three pairs of scenarios in the lying and sitting positions that are classified as the same type. Specifically, the combinations of Figures 6a, 7a and 8a, Figures 6a, 7b and 8a, and Figures 6a, 7c and 8a in the lying position correspond to the same type as Figures 6c, 7d and 8d, Figures 6c, 7e and 8d, and Figures 6c, 7f and 8d in the sitting position, respectively. Consequently, the action space is composed of 12 distinct types based on the section division principle, as outlined in Table 2.

Table 2. The 12 types of action spaces based on the classification method.

Type	Section Numbers	Combination of Figures 6–8	Demarcation Point and Arc Pair (from Bottom to Top)	Discriminant Condition ($y_{P14} - y_{P23} = l_1 \cdot \sin\alpha_{max} - l_1 \cdot \sin\alpha_{min} + l_2 \cdot \sin(\alpha_{max} + \beta_{min}) - l_2 \cdot \sin(\alpha_{min} + \beta_{max})$)	
1	3	Figures 6a, 7a and 8a Figures 6c, 7d and 8d	P_{34}-P_{23}-P_{14}-P_{12} C_4C_3-C_4C_2-C_1C_2	$y_{P14} - y_{P23} > 0$	(a). $\alpha_{min} = 50°$; $50° < \alpha_{max} \leq 90°$; (b). $\alpha_{min} = 50°$; $90° < \alpha_{max} \leq 130°$; $\beta_{max} \geq 180°$; (c). $\alpha_{min} = 0°$; $-90° \leq \beta_{min} < 0°$; Condition (a) and (b) are in lying position. Condition (c) is in sitting position.
2	3	Figures 6a, 7b and 8a Figures 6c, 7e and 8d	P_{34}-P_{14}-P_{23}-P_{12} C_4C_3-C_1C_3-C_1C_2	$y_{P14} - y_{P23} < 0$	
3	2	Figures 6a, 7c and 8a Figures 6c, 7f and 8d	P_{34}-$P_{14}(P_{23})$-P_{12} C_4C_3-C_1C_2	$y_{P14} - y_{P23} = 0$	
4	4	Figures 6a, 7a and 8b	P_{34}-P_{23}-P_{14}-P_{12}-Q_2 C_4C_3-C_4C_2-C_1C_2-C_2C_2	$y_{P14} - y_{P23} > 0$	(d). $\alpha_{min} = 50°$; $50° < \alpha_{max} \leq 90°$; $-\alpha_{max} - 85° \leq \beta_{max} \leq -\alpha_{max} + 90°$; $\beta_{max} \geq 180° - \alpha_{max} - \arccos(\frac{l_1}{l_2} \cdot \cos\alpha_{max})$; Condition (d) is in lying position.
5	4	Figures 6a, 7b and 8b	P_{34}-P_{14}-P_{23}-P_{12}-Q_2 C_4C_3-C_1C_3-C_1C_2-C_2C_2	$y_{P14} - y_{P23} < 0$	
6	3	Figures 6a, 7c and 8b	P_{34}-$P_{14}(P_{23})$-P_{12}-Q_2 C_4C_3-C_1C_2-C_2C_2	$y_{P14} - y_{P23} = 0$	
7	4	Figures 6a, 7a and 8c	P_{34}-P_{23}-P_{14}-Q_1-Q_2 C_4C_3-C_4C_2-C_1C_2-C_2C_2	$y_{P14} - y_{P23} > 0$	(e). $\alpha_{min} = 50°$; $90° < \alpha_{max} \leq 130°$; $-\alpha_{max} - 85° \leq \beta_{max} \leq -\alpha_{max} + 90°$; $\beta_{max} \geq 180° - \alpha_{max} - \arccos(\frac{l_1}{l_2} \cdot \cos\alpha_{max})$; Condition (e) is in lying position.
8	4	Figures 6a, 7b and 8c	P_{34}-P_{14}-P_{23}-Q_1-Q_2 C_4C_3-C_1C_3-C_1C_2-C_2C_2	$y_{P14} - y_{P23} < 0$	
9	3	Figures 6a, 7c and 8c	P_{34}-$P_{14}(P_{23})$-Q_1-Q_2 C_4C_3-C_1C_2-C_2C_2	$y_{P14} - y_{P23} = 0$	

Table 2. *Cont.*

Type	Section Numbers	Combination of Figures 6–8	Demarcation Point and Arc Pair (from Bottom to Top)	Discriminant Condition ($y_{P14} - y_{P23} = l_1 \cdot \sin\alpha_{max} - l_1 \cdot \sin\alpha_{min} + l_2 \cdot \sin(\alpha_{max} + \beta_{min}) - l_2 \cdot \sin(\alpha_{min} + \beta_{max})$)	
10	4	Figures 6b, 7d and 8d	Q_3-P_{34}-P_{23}-P_{14}-P_{12} C_3C_3-C_4C_3-C_4C_2-C_1C_2	$y_{P14} - y_{P23} > 0$	(f). $\alpha_{min} = 0°$; $-135° \leq \beta_{min} < -90°$; Condition (f) is in sitting position.
11	4	Figures 6b, 7e and 8d	Q_3-P_{34}-P_{14}-P_{23}-P_{12} C_3C_3-C_4C_3-C_1C_3-C_1C_2	$y_{P14} - y_{P23} < 0$	
12	3	Figures 6b, 7f and 8d	Q_3-P_{34}-$P_{14}(P_{23})$-P_{12} C_3C_3-C_4C_3-C_1C_2	$y_{P14} - y_{P23} = 0$	

Figure 6, Figure 7, and Figure 8, respectively, represent the various distributions of key points in the lower, middle, and upper regions. The table lists 12 types of action spaces, which are combinations included in Figures 6–8. The third column enumerates the combination cases corresponding to each type.

It is important to highlight that Types 1~3 have three conditions (a, b, and c) and are associated with two training postures (lying and sitting), whereas Types 4~12 are characterized by a single condition and a single training posture. Most significantly, within the action space of the same type, the group of linear trajectories exhibits identical rehabilitation characteristics and patterns for both the hip and knee joints, ensuring a consistent approach to rehabilitation across various patients in the same scenarios.

3.2. The Characteristics of Joint Rehabilitation Corresponding to the Rehabilitative Path

Points M and N are designated as the origin and terminus, respectively, of the linear trajectory L. The angles $\alpha_{L\max}$ and $\alpha_{L\min}$ represent the maximum and minimum hip flexion angles along trajectory L, while $\beta_{L\max}$ and $\beta_{L\min}$ denote the corresponding maximum and minimum knee extension angles. Furthermore, α_M and β_M are the hip and knee joint angles at the ankle's position M, and α_N and β_N are the respective angles at position N. The midpoint T of trajectory L is accompanied by angles α_T and β_T, which are the hip and knee joint angles when the ankle reaches T.

In the scenario where points M and N are located on different arcs C_iC_j (with $i \neq j$), as depicted in Figure 9a, point M is aligned with the maximum flexion angles for both the hip and knee joints, whereas point N corresponds to their minimum flexion angles. When M and N are situated on the same arc C_3C_3, point T represents the hip joint at its maximum flexion angle, with M and N indicating the minimum hip flexion angle. Concurrently, M and N correspond to the minimum and maximum knee extension angles, respectively, as shown in Figure 9b.

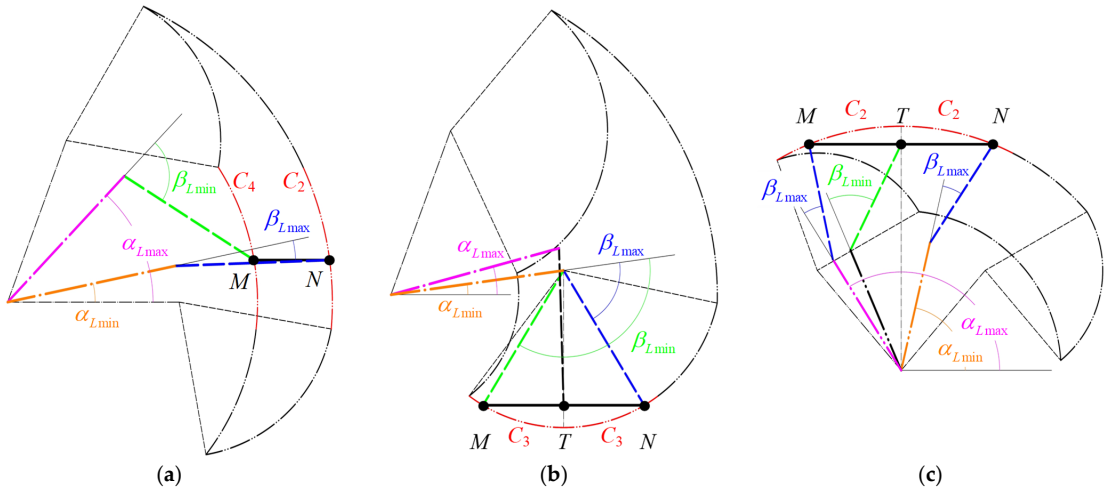

(**a**) (**b**) (**c**)

Figure 9. The positioning of the origin point M and the terminus point N of the linear trajectory: (**a**) M and N are on different arcs C_iC_j (with $i \neq j$); (**b**) M and N are on the same arc C_3C_3; (**c**) M and N are on the same arc C_2C_2.

In another configuration where M and N are on the same arc C_2C_2, M and N are associated with the maximum and minimum hip flexion angles, respectively. M and N also correspond to the maximum knee extension angle, while point T is at the minimum knee extension angle, as illustrated in Figure 9c. The limiting conditions for the joint angles corresponding to the linear trajectory in these three cases can be articulated as follows:

$$\begin{cases} \alpha_{Lmax} = \alpha_M; \alpha_{Lmin} = \alpha_N; \beta_{Lmax} = \beta_N; \beta_{Lmin} = \beta_M; (C_iC_j, i \neq j) \\ \alpha_{Lmax} = \alpha_T; \alpha_{Lmin} = \alpha_M = \alpha_N; \beta_{Lmax} = \beta_N; \beta_{Lmin} = \beta_M; (C_iC_j, i = j = 3) \\ \alpha_{Lmax} = \alpha_M; \alpha_{Lmin} = \alpha_N; \beta_{Lmax} = \beta_M = \beta_N; \beta_{Lmin} = \beta_T; (C_iC_j, i = j = 2) \end{cases} \quad (5)$$

For a detailed analysis of the joint rehabilitation features and patterns within various action spaces for the linear trajectory groups, Type 10 has been discussed. This targeted study aims to offer physicians a comprehensive guide and theoretical underpinning for the effective utilization of rehabilitation robots in their practice.

Moreover, drawing from the analytical findings of the selected types, we have crafted a comprehensive summary of the joint rehabilitation characteristics and principles applicable to the remaining types. This compilation aims to serve as a reference for healthcare professionals, enhancing their ability to tailor joint rehabilitation protocols to the specific needs of individual patients.

Let us consider Type 10 as a case study. We have configured the hip joint's motion range to span from 0° to 70° and the knee joint's motion range from −135° to −18°. Additionally, the lengths of the thigh and calf have been standardized at 400 mm and 360 mm, respectively. With these parameters, the action space is graphically represented in Figure 10a, which is segmented into four distinct regions (green, yellow, pink, and blue), setting nine exemplary linear trajectories, l_1 through l_9, arranged vertically from bottom to top. An analysis of the joint rehabilitation characteristics corresponding to these trajectories follows.

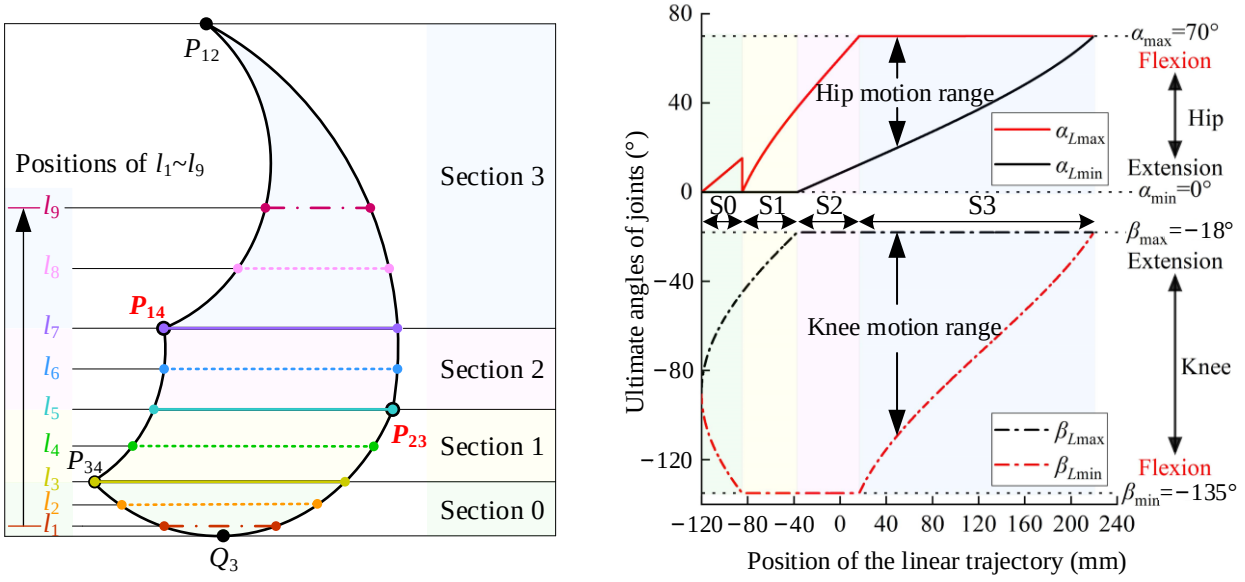

Figure 10. The positions and the ultimate joint angles of the linear trajectories within the action space of Type 10: (**a**) the nine linear trajectories (l_1~l_9) from bottom to top; (**b**) the ultimate angles of joints corresponding to the position of the linear trajectories.

The interplay between the linear trajectory's position (y_l) and the maximum flexion–extension angles of the hip and knee joints is depicted in Figure 10b. The hip joint's position is established as the coordinate origin, with the horizontal axis denoting the trajectory's height and the vertical axis representing the joint angles. As delineated in Equation (7),

the linear trajectory will correspond to the hip joint's maximum flexion motion when $\alpha_{L\max} = \alpha_{\max}$. Similarly, the linear trajectory will correspond to the knee joint's maximum flexion motion when $\beta_{L\min} = \beta_{\min}$. An ultimate joint motion range is achieved when the maximum motion range of the patient's joints matches that of the linear trajectory.

$$\begin{cases} \alpha_{\min} \le \alpha_{L\min} \le \alpha_{L\max} \le \alpha_{\max} \\ \beta_{\min} \le \beta_{L\min} \le \beta_{L\max} \le \beta_{\max} \end{cases} \tag{6}$$

In the early stages of recovery, the emphasis of rehabilitation is placed on regaining muscle strength, making it crucial to engage in exercises that involve a wide range of joint motion. As patients progress into the middle or late stages of recovery, the focus shifts toward ensuring the joints can extend freely. At this point, the ultimate flexion training of the joints becomes particularly significant to enhance their functional capabilities and restore full mobility. As shown in Figure 10b, we analyze the influence of the linear trajectory's section and position on the characteristics of joint rehabilitation.

As shown in Figure 10b, it is evident that the trajectory within section 0 (denoted by the green area) lacks both the broad joint motion range and the capacity for ultimate joint flexion. Consequently, section 0 is not an appropriate choice for planning linear trajectories aimed at joint rehabilitation training.

Moving on to section 1 (the yellow area), as the trajectory ascends, there is a gradual expansion in the joints' range of motion. Notably, the knee joint maintains its ultimate flexion ($\beta_{L\min} = \beta_{\min}$). Thus, the linear trajectories in section 1 are best suited for rehabilitation that emphasizes the knee joint as the primary focus, with the hip joint serving as a supportive element. In summary, the trajectories in section 1 preserve the knee joint's ultimate flexion, and as the trajectory's position rises, the intensity of joint training correspondingly increases.

Moving on to section 2 (the pink area), the trajectory's upward movement is accompanied by the knee joint maintaining both ultimate flexion and maximum range of motion ($\beta_{L\max} = \beta_{\max}$ and $\beta_{L\min} = \beta_{\min}$). Additionally, the hip joint's flexion angle and motion range increase progressively. Therefore, the linear trajectories in section 2 continue to prioritize the knee joint for rehabilitation, with the hip joint in a supportive role. In conclusion, the trajectories in section 2 sustain the knee joint's ultimate flexion and maximum motion range, and the higher the trajectory's position, the more intense the joint training becomes.

Lastly, in section 3 (the blue area), the trajectory's ascent is characterized by the hip joint maintaining ultimate flexion ($\alpha_{L\max} = \alpha_{\max}$) and a diminishing motion range. The knee joint's motion range also decreases, and its ultimate flexion capability is lost. Moreover, the length of the linear trajectory is reduced. Under equivalent training conditions of speed and duration, the frequency of the hip joint's ultimate flexion increases, enhancing the efficiency of the training of the hip joint. Thus, the linear trajectories in section 3 are designed with the hip joint as the primary focus and the knee joint as a supportive element. In conclusion, the higher the trajectory's position, the more effective the training efficiency for the hip joint's ultimate flexion.

We have identified five key metrics to evaluate the joint rehabilitation effectiveness of the nine linear trajectories (l_1~l_9), as depicted in Figure 11a,b. These metrics include the ultimate hip joint flexion angle, the ultimate knee joint flexion angle, the maximum hip joint motion range, the maximum knee joint motion range, and the ultimate joint flexion frequency.

Specifically, linear trajectories l_1 and l_2 do not encompass the joints' maximum motion range or ultimate flexion. Trajectories l_3 and l_4 are characterized by the inclusion of the knee joint's ultimate flexion only. Trajectories l_5 and l_6 extend to include both the knee joint's ultimate flexion and its maximum motion range. Trajectory l_7 is distinguished by encompassing the knee joint's ultimate flexion and maximum motion range, as well as the hip joint's ultimate flexion. Furthermore, the training frequency for trajectories l_1 through l_7 is essentially uniform. Trajectories l_8 and l_9 exclusively feature the hip joint's ultimate flexion, with l_9 exhibiting the highest training frequency among all trajectories,

indicating that, under identical training conditions, l_9 achieves the greatest number of hip joint flexions.

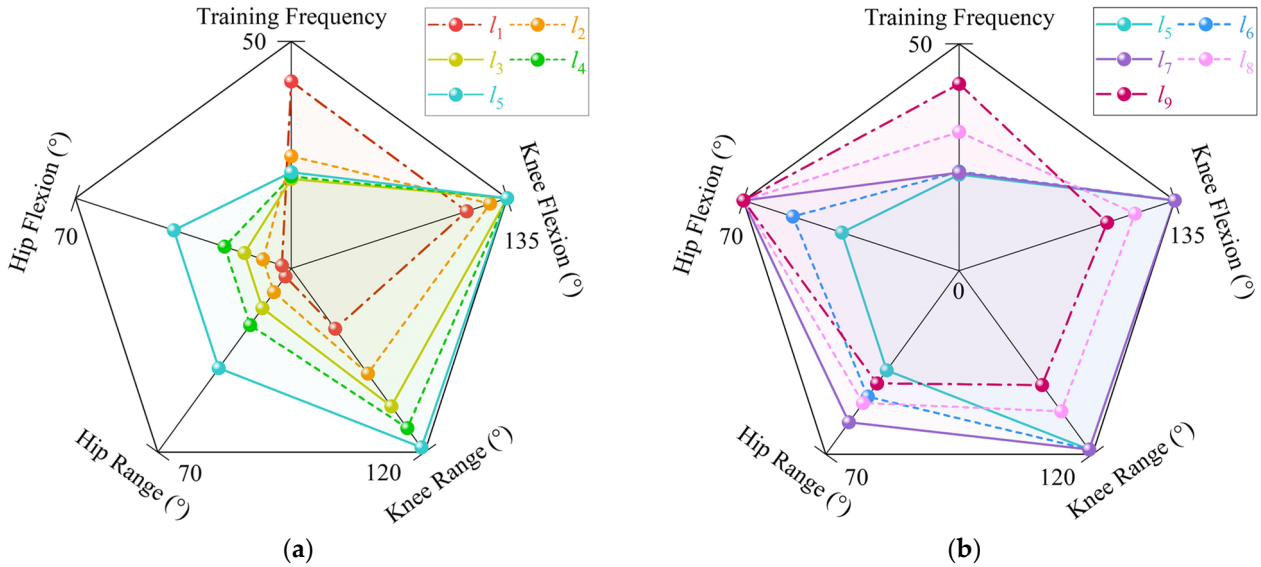

Figure 11. The five key metrics to evaluate joint rehabilitation of linear trajectories: (**a**) the key metrics of joint rehabilitation of l_1~l_5; (**b**) the key metrics of joint rehabilitation of l_5~l_9.

It can be concluded that trajectory l_7 is the optimal choice for comprehensive joint rehabilitation, as it includes the knee joint's ultimate flexion, maximum motion range, and the hip joint's ultimate flexion. Trajectories l_8 and l_9 are designed for enhanced efficiency in hip joint ultimate flexion. Trajectories l_5 and l_6, which include both the knee joint's ultimate flexion and maximum motion range, offer a more intensive training focus on the hip joint. Trajectories l_3 and l_4, focusing solely on the knee joint's ultimate flexion, provide a lower intensity of training for the hip joint. Lastly, trajectories l_1 and l_2 have minimal rehabilitative impact on the joints.

Following the analytical approach applied to Type 10, each of the remaining types can also be categorized into three effective training sections (sections 1 to 3) and one ineffective training section (section 0). Across all types (from Type 1 to Type 12), the starting point M and the ending point N of the linear trajectory are located on distinct curves of C_iC_j (where $i \neq j$) when the trajectory falls within the effective sections. Conversely, when the trajectory is in the ineffective section, both points M and N are situated on the same curve of C_iC_j.

Drawing from the 12 distinct types of action spaces, we have distilled a set of universal characteristics and patterns that define the linear trajectories for joint rehabilitation. This comprehensive summary provides a foundational framework for understanding the nuances of effective rehabilitation strategies across various patient scenarios and recovery stages.

In the ineffective section 0, the linear trajectory fails to encompass the joint's ultimate flexion or its maximum motion range, rendering it ineffective for joint rehabilitation purposes.

In the effective section 1, the linear trajectory exclusively includes the knee joint's ultimate flexion, which can manifest in two scenarios. If section 0 is positioned at the bottom of the action space, as the linear trajectory ascends, there is an increase in the knee joint's motion range, the hip joint's maximum flexion angle, and the hip joint's motion range, leading to enhanced training intensity. Conversely, when section 0 is at the top or absent, the frequency of the knee joint's ultimate flexion diminishes under constant speed and time conditions. Thus, the linear trajectory in section 1 primarily targets knee joint rehabilitation with supplementary hip joint involvement.

In the effective section 2, the linear trajectory encompasses three distinct situations. When $y_{P14} > y_{P23}$, the trajectory includes both the knee joint's ultimate flexion and its maximum motion range. Additionally, as the trajectory's position elevates, both the hip joint's ultimate flexion and maximum motion range increase. When $y_{P14} < y_{P23}$, the trajectory includes the hip joint's ultimate flexion and maximum motion range, with a concurrent increase in the knee joint's maximum flexion angle and maximum motion range as the trajectory rises. When $y_{P14} = y_{P23}$, the effective section 2 can be considered a singular line with P_{14} as the starting point and P_{23} as the end point, encompassing the ultimate flexion and motion range of both joints.

Lastly, in the effective section 3, the trajectory solely includes the hip joint's ultimate flexion, presenting two scenarios. If section 0 is at the bottom or absent, the frequency of the hip joint's ultimate flexion decreases as the trajectory's position increases under the same speed and time. When section 0 is at the top, the hip joint's motion range, the knee joint's maximum flexion angle, and the knee joint's motion range all increase, leading to more intensive training. Consequently, the linear trajectory in section 3 is primarily focused on hip joint rehabilitation with supplementary knee joint involvement.

As shown in Table 3, the influence of the linear trajectory's sectional division on joint rehabilitation is universally applicable across all types, ensuring a tailored approach to accommodate the varying needs of patients. This systematic categorization into effective and ineffective training sections allows for precise calibration of the rehabilitation process, optimizing the trajectory's design to enhance joint recovery and function. By leveraging this comprehensive framework, clinicians can effectively tailor rehabilitation programs to achieve the best possible outcomes for patients at different stages of recovery.

Table 3. The relationship between joint rehabilitation requirements and the positions of linear trajectories applicable to all types of action spaces.

Type 1~12	Primary Indicators of Joint Rehabilitation		Auxiliary Indicators of Joint Rehabilitation	
	Relationship of P_{14} and P_{23}	Change Rules as Position Rises	Position of Section 0	Change Rules as Position Rises
section 0	/	/	/	/
section 1	All is permissible	$\beta_{L\min} = \beta_{\min}$	At top or not exist	Hip flexion frequency increases.
			At bottom	$\alpha_{L\max}$, $\alpha_{L\min}$ and $\beta_{L\max}$ increase.
section 2	$y_{P14} > y_{P23}$	$\beta_{L\max} = \beta_{\max}$; $\beta_{L\min} = \beta_{\min}$	All is permissible	$\alpha_{L\max}$ and $\alpha_{L\min}$ increase.
	$y_{P14} < y_{P23}$	$\alpha_{L\max} = \alpha_{\max}$; $\alpha_{L\min} = \alpha_{\min}$		$\beta_{L\max}$ and $\beta_{L\min}$ increase.
	$y_{P14} = y_{P23}$	$\alpha_{L\max} = \alpha_{\max}$; $\alpha_{L\min} = \alpha_{\min}$; $\beta_{L\max} = \beta_{\max}$; $\beta_{L\min} = \beta_{\min}$		Not exist
section 3	All is permissible	$\alpha_{L\max} = \alpha_{\max}$	At top or not exist	$\alpha_{L\min}$, $\beta_{L\max}$ and $\beta_{L\min}$ increase.
			At bottom	Knee flexion frequency increases.

It is a summary of the relationship between the joint rehabilitation characteristics and the positions of linear trajectories under all 12 types of action spaces. This allows physicians to quickly identify the specific section and the position of the corresponding linear trajectory based on the set joint rehabilitative requirements.

3.3. Generation of Rehabilitation Path

It is challenging for physicians to directly plan rehabilitative trajectories based on the joint rehabilitation needs they design because they cannot intuitively plan matching trajectories within the action space. Therefore, this paper proposed a rehabilitation system that enables physicians to plan trajectories based on joint training indicators according to the types of patient's action space, as illustrated in Figure 12. Moreover, the action space and the coordinates of the linear trajectory on the display panel are obtained based on Equation (3). Five joint rehabilitation indicators were considered and provided on the control panel for physician adjustment. These include the range of motion of the hip joint,

the range of motion of the knee joint, the degree of hip joint flexion, the degree of knee joint flexion, and flexion frequency. Physicians customize five joint training parameters for the patient's rehabilitation by adjusting the five corresponding controls on the operation panel. Subsequently, the system generates the corresponding trajectory based on the joint rehabilitation requirements set by the physician.

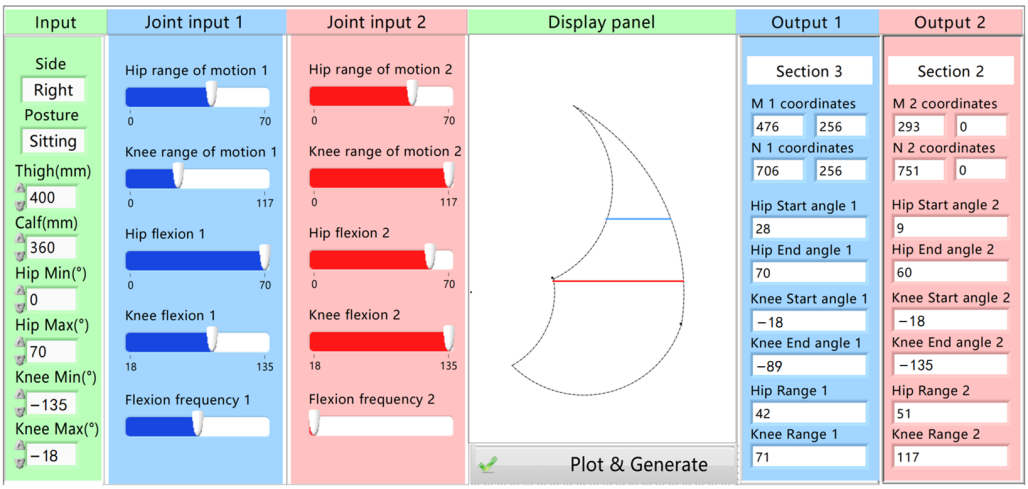

Figure 12. Operating system for generating linear rehabilitation paths based on joint rehabilitation indicators.

Once the physician enters the lower-limb parameters of the patient in the first column, including leg length and joint mobility, the system generates a corresponding action space on the board. Concurrently, the joint rehabilitation indicator adjustment controls are designed to update in real time to match the patient's current joint mobility. Recognizing that it is challenging for physicians to plan corresponding rehabilitation paths on the user interface based on the formulated joint rehabilitative requirements, the system incorporates the relationship between joint rehabilitation indicators and trajectories. This is to generate a matching rehabilitation path, as analyzed earlier. By setting five joint rehabilitation indicators in the second column, the system automatically generates a matching trajectory, assisting the physician in creating a straight-line trajectory that matches the setting joint rehabilitation needs. Both the motion space and the straight trajectory are depicted in the third column. Finally, the panel displays the maximum and minimum flexion angles of the joints, the range of motion of the joint, and the interval where the straight-line trajectory lies. This comprehensive integration of physiological inputs and system-generated trajectories allows for a more effective and customized joint rehabilitation plan tailored to the patient's specific requirements and facilitates the rehabilitation process.

4. Rehabilitative Trajectory Planning-Based Jerk Minimization

4.1. Polynomial Trajectory Planning

Based on the initial and final position of the rehabilitation trajectory generated by the joint rehabilitative indicators, different paths with different motion parameters by the robot end effector can be generated [41]. It is common to split the trajectory into multiple segments, as shown in Figure 13. There are $N+1$ key points $P_i(0 \leq i \leq N)$ on the trajectory to connect the adjacent segments. The rehabilitation trajectory can be represented by polynomials with k-segments. Every single segment can be expressed by a polynomial of degree n, written as

$$f(t) = p_0 + p_1 t + p_2 t^2 + \cdots + p_n t^n. \quad (7)$$

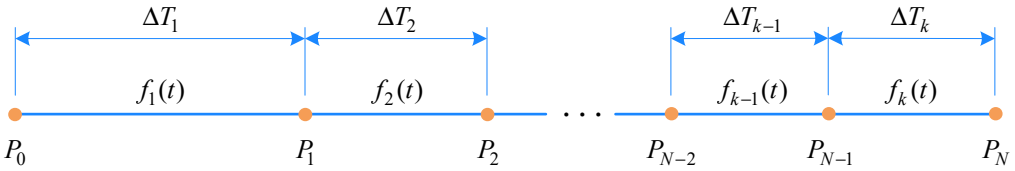

Figure 13. The trajectory composed of multiple segments.

Through writing the nth-order coefficients in a vector form $p = [p_0 \quad p_1 \quad \cdots \quad p_n]^\top$, and then differentiating them, the trajectory of a single segment, as well as the velocity, acceleration, and the jerk can be represented as

$$\begin{aligned} p(t) = f(t) &= \begin{bmatrix} 1 & t & t^2 & t^3 & t^4 & t^5 & \cdots & t^n \end{bmatrix} p = Pp \\ v(t) = f'(t) &= \begin{bmatrix} 0 & 1 & 2t & 3t^2 & 4t^3 & 5t^4 & \cdots & nt^{n-1} \end{bmatrix} p = Vp \\ a(t) = f''(t) &= \begin{bmatrix} 0 & 0 & 2 & 6t & 12t^2 & 20t^3 & \cdots & \frac{n!}{(n-2)!}t^{n-2} \end{bmatrix} p = Ap \\ j(t) = f'''(t) &= \begin{bmatrix} 0 & 0 & 0 & 6 & 24t & 60t^2 & \cdots & \frac{n!}{(n-3)!}t^{n-3} \end{bmatrix} p = Jp \end{aligned} \cdot \tag{8}$$

The whole trajectory in Figure 13 is separated into multiple segments connected by the key points, and it can be expressed as a multi-segment trajectory. The i-th segment is written as

$$f_i(t) = \begin{bmatrix} 1 & t & t^2 & \cdots & t^n \end{bmatrix} p_i, \quad t_{i-1} \le t < t_i, \quad i = 1, 2, \cdots, k \tag{9}$$

where $t_i - t_{i-1}$ is the execution time, which is equal to the proportion of the length of the i-th segment, k is the number of segments, and $p_i = \begin{bmatrix} p_{i0} & p_{i1} & \cdots & p_{in} \end{bmatrix}^\top$ is the parameters of polynomials of the k-th segment.

4.2. Trajectory Optimization

In traditional rehabilitation therapies, physicians commonly drag the patient's foot to complete the end linear motion of flexion–extension of the lower limbs. During this process, they provide small shock, smooth, and stable rehabilitation trajectories through manual techniques and experience. To reduce the impact and vibration of lower-limb rehabilitation robots and track smoother and more stable trajectories, the impact along the trajectory will be minimized, and a target function represented in a quadratic form is constructed as

$$\min \quad j_i^2(t) = (f'''(t))^2. \tag{10}$$

By combining the objective function with Equation (9), we can obtain

$$\begin{aligned} \int_0^T (f'''(t))^2 dt &= \sum_{i=1}^{k} \int_{t_{i-1}}^{t_i} (f^{(3)}(t))^2 dt \\ &= \sum_{i=1}^{k} \int_{t_{i-1}}^{t_i} \left[(J_i p)^\top (J_i p) \right] dt \\ &= \sum_{i=1}^{k} p^T \int_{t_{i-1}}^{t_i} (J_i{}^\top J_i) dt \cdot p = \sum_{i=1}^{k} p^T Q_i p \end{aligned} \quad . \tag{11}$$

In the equation, Q_i is a block matrix, and it can be expressed as

$$Q_i = \int_{t_{i-1}}^{t_i} J^T J dt = \begin{bmatrix} 0_{3\times 3} & 0_{3\times(n-2)} \\ 0_{(n-2)\times 3} & \frac{(r-1)(r-2)(r-3)(c-1)(c-2)(c-3)}{(r+c-7)}(t_i^{r+c-7} - t_{i-1}^{r+c-7}) \end{bmatrix}, \tag{12}$$

where r and c stand for the row and column indices of the matrix, respectively. It is seen that the fourth block of Q_i is a none-zero entry, which is expressed in the form of a diagonal matrix:

$$Q = diag\begin{bmatrix} Q_1 & Q_2 & \cdots & Q_k \end{bmatrix}. \tag{13}$$

In traditional rehabilitation therapies, physicians tend to impose certain limitations on the starting and ending points of the rehabilitation trajectory as well as ensure the continuity of the trajectory. Thus, assuming that at the initial point in the first segment of the trajectory, the initial position, velocity, and acceleration equal to p_0, v_0, and a_0, respectively, the corresponding constraints can be set to

$$\begin{array}{l} p(t_0) = \begin{bmatrix} 1 & t_0 & t_0^2 & t_0^3 & t_0^4 & t_0^5 & \cdots & t_0^n \end{bmatrix} p_1 = P_0 p_1 = p_0 \\ v(t_0) = \begin{bmatrix} 0 & 1 & 2t_0 & 3t_0^2 & 4t_0^3 & 5t_0^4 & \cdots & nt_0^{n-1} \end{bmatrix} p_1 = V_0 p_1 = v_0 \\ a(t_0) = \begin{bmatrix} 0 & 0 & 2 & 6t_0 & 12t_0^2 & 20t_0^3 & \cdots & n(n-1)t_0^{n-2} \end{bmatrix} p_1 = A_0 p_1 = a_0 \end{array} . \quad (14)$$

Similarly, for the ending point of the last segment of the trajectory, the position, velocity, and acceleration constraints can also be specified. To ensure the continuity of the trajectory, the position, velocity, and acceleration of the end point of the current segment are set to be equal to those of the starting point of the next segment. This approach allows for a seamless transition from one movement phase to the next, facilitating smooth and effective rehabilitation processes. The constraint equations for the intersection of two adjacent trajectories can be represented as

$$\begin{array}{l} p_j(t_i) = P_i p_j = P_i p_{j+1} = p_{j+1}(t_i) \\ v_j(t_i) = V_i p_j = V_i p_{j+1} = v_{j+1}(t_i) \\ a_j(t_i) = A_i p_j = A_i p_{j+1} = a_{j+1}(t_i) \end{array} . \quad (15)$$

The kinematic constraint equations of all the key points mentioned above can be transformed into a huge overarching matrix, which is represented as

$$\begin{bmatrix} 1, t_0, t_0^2, \cdots, t_0^n, 0_{1\times(k-1)(n+1)} \\ 0, 1, 2t_0, \cdots, nt_0^{n-1}, 0_{1\times(k-1)(n+1)} \\ 0, 0, 2, \cdots, n(n-1)t_0^{n-2}, 0_{1\times(k-1)(n+1)} \\ \vdots \\ 0_{1\times(i-1)(n+1)}, 1, t_i, t_i^2, \cdots t_i^n, 0_{1\times(k-i)(n+1)} \\ \vdots \\ 0_{1\times(k-1)(n+1)}, 1, t_k, t_k^2, \cdots, t_k^n \\ 0_{1\times(k-1)(n+1)}, 0, 1, 2t_k, \cdots, nt_k^{n-1} \\ 0_{1\times(k-1)(n+1)}, 0, 0, 2, \cdots, n(n-1)t_k^{n-2} \\ \vdots \\ 0_{1\times(i-1)(n+1)}, 1, t_i, t_i^2, \cdots, t_i^n, -1, -t_i, -t_i^2, \cdots, -t_i^n, 0_{1\times(k-i-1)(n+1)} \\ 0_{1\times(i-1)(n+1)}, 0, 1, 2t_i, \cdots, nt_i^{n-1}, 0, -1, -2t_i, \cdots, -nt_i^{n-1}, 0_{1\times(k-i-1)(n+1)} \\ 0_{1\times(i-1)(n+1)}, 0, 0, 2, \cdots, n(n-1)t_i^{n-2}, 0, 0, -2, \cdots, -n(n-1)t_i^{n-2}, 0_{1\times(k-i-1)(n+1)} \\ \vdots \end{bmatrix} \cdot p = \begin{bmatrix} p_0 \\ v_0 \\ a_0 \\ \vdots \\ p_i \\ \vdots \\ p_N \\ v_N \\ a_N \\ \vdots \\ 0 \\ 0 \\ 0 \\ \vdots \end{bmatrix} . \quad (16)$$

Based on Equations (11) and (13), the problem of solving the jerk is simplified as a quadratic programming problem: $\sum_{i=1}^{k} j_i = p^T Q p$. Among them, vector p represents the sum of n-th degree polynomial coefficients of k trajectory segments, including k*(n + 1) coefficients to be solved. Q represents the summary of the matrix Q_i for each trajectory segment, which is a symmetric matrix considered the Hessian matrix for the quadratic programming problems. According to Equation (12), since $r \geq 4$, $c \geq 4$, and $t_i > t_{i-1}$, it can be determined that Q is a semi-positive definite matrix. Therefore, the problem of solving the minimum jerk can be regarded as a convex quadratic programming problem, and there exists a global optimal solution.

On this basis, an optimization function $quadprog(Q, p, [], [], A_{eq}, b_{eq})$ was used in MATLAB R2022a to solve quadratic programming problems, where Q is the Hessian matrix

in quadratic programming, corresponding to Equation (13). p represents the summary of n-th degree polynomial coefficients for k trajectory segments. The coefficient matrix and the right-hand vector of the linear inequality constraint represented by items 3 and 4 do not exist and are therefore set to be empty. A_{eq} represents the coefficient matrix of linear equality constraints, corresponding to the large matrix of the first term on the left side of Equation (16). b_{eq} represents the right-hand vector of the linear equality constraint, corresponding to the vector on the right-hand side of Equation (16). Finally, based on the equality constraint conditions and the quadratic term matrix, the coefficient vector of the first-order term in the quadratic programming that minimizes the total jerk can be obtained, which is the n-th degree polynomial coefficient of each trajectory segment.

4.3. Generation of Rehabilitation Trajectory

As shown in Figure 14, the jerk minimization trajectory planning is applied to the rehabilitation robot system, which is controlled using the LabView software (NI LabVIEW 2018). In the experiment, the motion information of the robot joints, such as joint displacement and velocity, is read from the encoder of the motor, with its main technology parameters shown in Figure 15. Furthermore, the acceleration and jerk can be obtained by performing once and twice differentiations on the encoder's angular velocity, respectively. Multiple repeated experiments were conducted to calculate the average value, aiming to minimize the deviations. The motion of the end effector is calculated through forward kinematics.

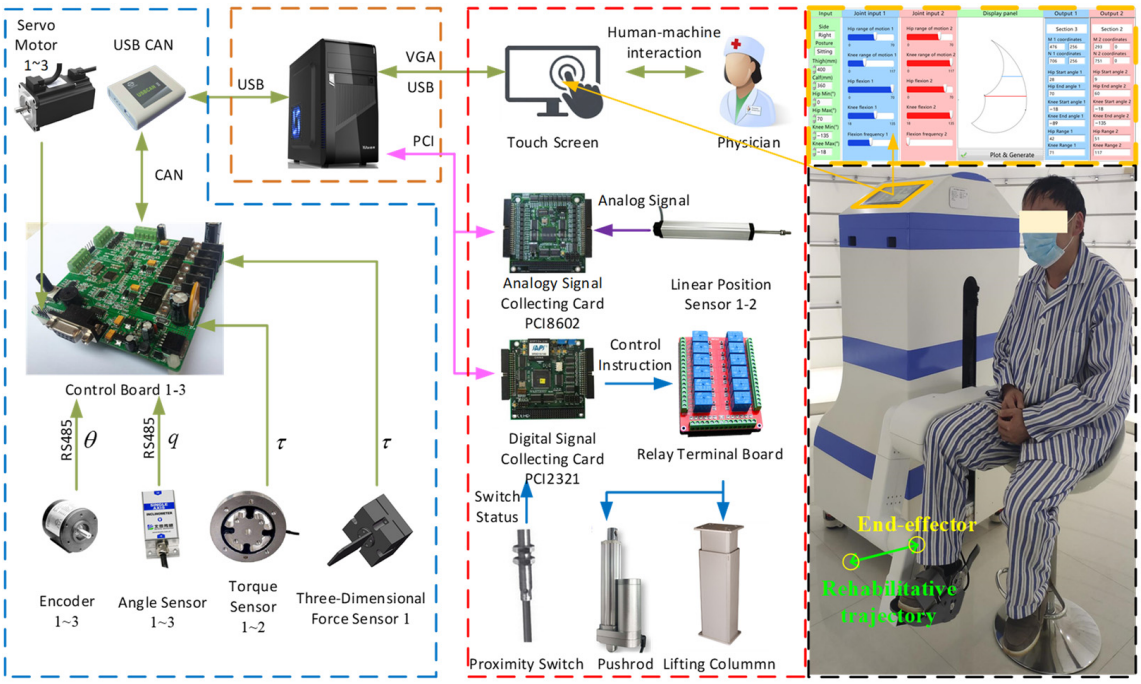

Figure 14. Hardware system and experimental platform for trajectory tracking.

Main Technology Parameters
Style-Nr: EB38A6-L6PR-1000
Operating principle: Incremental
Resolution ratio: 1000
Starting torque: No more than 1Nm
Maximum speed: 3000r/min
Operating Temperature: -40~+100°C
Maximum axial load radial/axial: 19.6/9.8N

Figure 15. Main technology parameters of the encoder.

Based on the rehabilitation needs for joints, the initial position is set at the end point of the linear trajectory located far from the hip joint. Analogous to the traditional therapeutic approach where physicians drag the affected limb, a complete cycle of linear rehabilitation exercise involves a single flexion and extension of the lower limb, corresponding to the robot's end effector moving from point N to point M and then returning to point N. The coordinates of key points of the two trajectories in Figure 12 are shown in Table 3. Subsequently, the linear rehabilitation trajectory is composed of 14 segments, and a seventh-order polynomial is used from the perspective of impact continuity and time consumption. Then, the Cartesian coordinate representation of each segment is expressed as

$$\{x_i(t_i), y_i(t_i)\} = p_0 + p_1 t_i + p_2 t_i^2 + p_3 t_i^3 + p_4 t_i^4 + p_5 t_i^5 + p_6 t_i^6 + p_7 t_i^7 \quad (17)$$

It is set that the distance between key points is equal. The estimated execution time for the robot's operation is set to TE_1 = 8.4 s and TE_2 = 16.8 s, respectively, based on the proportional relationship between the lengths of the two trajectories. The trajectory optimization problem is solved using the MATLAB quadprog optimization algorithm (the quadratic programming solver). The random trajectories are also generated using a seventh-order polynomial method, with constraints set on the initial and terminal points of the trajectory, as well as the first and last points of adjacent trajectories. However, the minimization of jerk is not the objective, which implies that it does not involve quadratic programming problems. Table 4 represents the coordinates of the key points. All trajectories pass through the same key points and can both achieve linear rehabilitative trajectories, but there are differences in the outlines.

Table 4. The key points for the two trajectories of the rehabilitation robot.

No.	0	1	2	3	4	5	6	7	8	9	10	11	12	13	14
$^{(1)}P_i$	$\begin{bmatrix}0.71\\0.26\end{bmatrix}$	$\begin{bmatrix}0.67\\0.26\end{bmatrix}$	$\begin{bmatrix}0.64\\0.26\end{bmatrix}$	$\begin{bmatrix}0.61\\0.26\end{bmatrix}$	$\begin{bmatrix}0.57\\0.26\end{bmatrix}$	$\begin{bmatrix}0.54\\0.26\end{bmatrix}$	$\begin{bmatrix}0.51\\0.26\end{bmatrix}$	$\begin{bmatrix}0.48\\0.26\end{bmatrix}$	$\begin{bmatrix}0.51\\0.26\end{bmatrix}$	$\begin{bmatrix}0.54\\0.26\end{bmatrix}$	$\begin{bmatrix}0.57\\0.26\end{bmatrix}$	$\begin{bmatrix}0.61\\0.26\end{bmatrix}$	$\begin{bmatrix}0.64\\0.26\end{bmatrix}$	$\begin{bmatrix}0.67\\0.26\end{bmatrix}$	$\begin{bmatrix}0.71\\0.26\end{bmatrix}$
$^{(2)}P_i$	$\begin{bmatrix}0.75\\0\end{bmatrix}$	$\begin{bmatrix}0.69\\0\end{bmatrix}$	$\begin{bmatrix}0.62\\0\end{bmatrix}$	$\begin{bmatrix}0.55\\0\end{bmatrix}$	$\begin{bmatrix}0.49\\0\end{bmatrix}$	$\begin{bmatrix}0.42\\0\end{bmatrix}$	$\begin{bmatrix}0.36\\0\end{bmatrix}$	$\begin{bmatrix}0.29\\0\end{bmatrix}$	$\begin{bmatrix}0.36\\0\end{bmatrix}$	$\begin{bmatrix}0.42\\0\end{bmatrix}$	$\begin{bmatrix}0.49\\0\end{bmatrix}$	$\begin{bmatrix}0.55\\0\end{bmatrix}$	$\begin{bmatrix}0.62\\0\end{bmatrix}$	$\begin{bmatrix}0.69\\0\end{bmatrix}$	$\begin{bmatrix}0.75\\0\end{bmatrix}$

The units of coordinates are all in meters.

The comparison of the computational time between the optimized and randomly generated trajectories is shown in Figure 16. Mostly, the computational time of the optimized trajectory is about three times higher than the one without optimization. Despite all this, the computation time of optimization is short enough to be accepted in real robot rehabilitation.

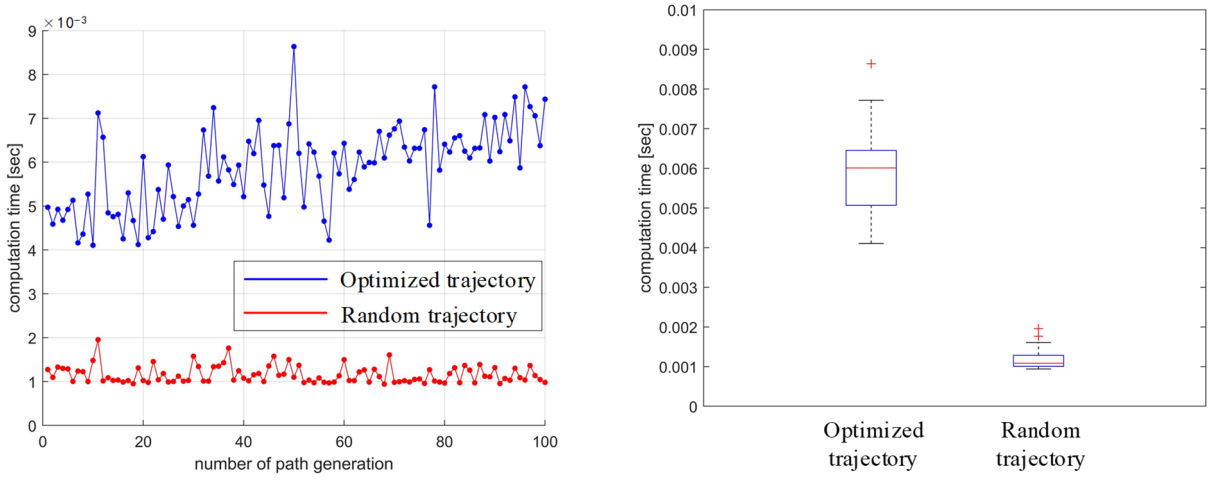

(**a**) (**b**)

Figure 16. The computational time of trajectory generation: (**a**) line chart; (**b**) box chart.

Figure 17 shows the position, velocities, accelerations, and jerks of the robot's end effector in Cartesian space, which means that the optimized trajectories can ensure smaller and more continuous jerks compared with the randomly generated ones. Besides differing from the random trajectories, it conforms more closely to the trajectory characteristics during traditional rehabilitation trajectories by the physicians dragging the affected limb. The corresponding polynomial coefficients and execution times for the optimized trajectories in each segment on the x-axis are shown in Table 5. Evidently, the two rehabilitation paths generated based on two joint rehabilitative indicators have distinct end effector displacement. It is relatively challenging for physicians to accurately plan the matching rehabilitation path solely based on the set of joint rehabilitative indicators.

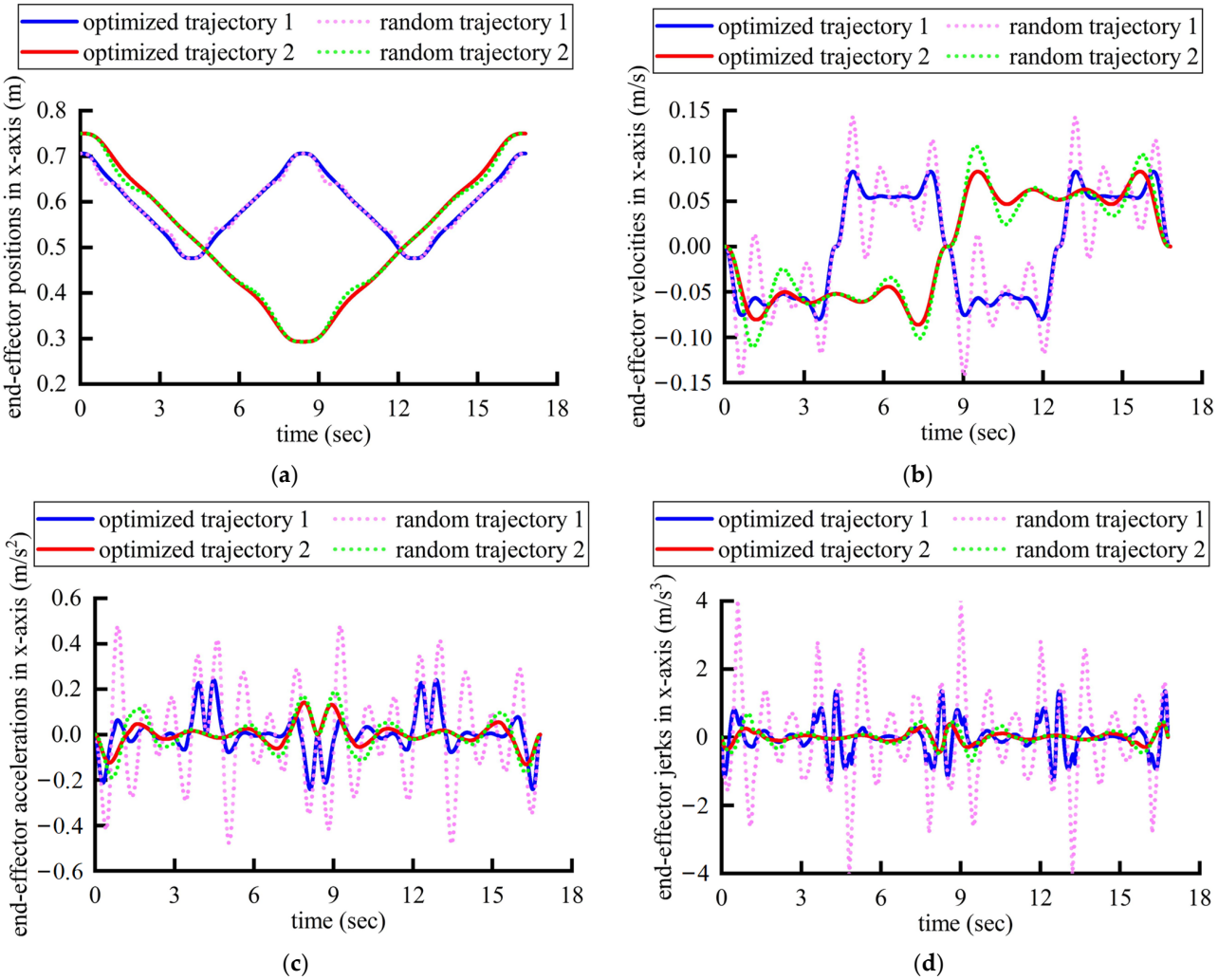

Figure 17. The motion data of the robot's end effector in Cartesian space: (**a**) positions; (**b**) velocities; (**c**) accelerations; (**d**) jerks.

The discrete coordinates of several points on the robot's end effector trajectory, which have been optimized from the previous section, are subjected to the kinematic inverse solution. This yields the angular displacements at the hip and knee joints corresponding to these points. Subsequently, these angular displacements are input into the motor controller, where they are processed through a PD control algorithm to achieve the rehabilitation trajectory planned earlier. The angular displacements, angular velocities, angular accelerations, and jerks for the hip and knee joints are shown in Figure 18. It can be observed that the joint angular velocity and angular acceleration curves achieved through the seventh-order polynomial planning are both smooth and continuous. The jerk curves show that

the starting and the ending positions of the joint exhibit zero jerk, aligning well with the lower-limb rehabilitation requirements of the patient.

Table 5. Polynomial coefficients and execution time in each segment of the two trajectories.

Segs	Coefficients $[\ p_0,\ p_1,\ p_2,\ p_3,\ p_4,\ p_5,\ p_6,\ p_7\ ]$	t_i (s)
1	${}^{(1_x)}\mathrm{p}_1$: [0.7500 0 0 0 −1.9103 4.7426 −4.4070 1.4838]	0.70
	${}^{(2_x)}\mathrm{p}_1$: [0.7500 0 0 0 −0.1632 0.2185 −0.1093 0.0198]	1.35
2	${}^{(1_x)}\mathrm{p}_2$: [0.6847 −0.1469 0.0389 0.1942 −0.7588 1.3593 −1.4602 0.6930]	0.50
	${}^{(2_x)}\mathrm{p}_2$: [0.6847 −0.0778 0.0145 0.0325 −0.0578 0.0474 −0.0239 0.0054]	1.15
3	${}^{(1_x)}\mathrm{p}_3$: [0.6194 −0.1165 −0.0270 −0.0299 0.1111 0.0264 −0.1580 0.0765]	0.60
	${}^{(2_x)}\mathrm{p}_3$: [0.6194 −0.0523 −0.0086 −0.0061 0.0091 $4.7142e-04$ −0.0025 $5.7441e-04$]	1.10
4	${}^{(1_x)}\mathrm{p}_4$: [0.5541 −0.1221 0.0316 0.0241 −0.1049 0.0718 −0.0174 0.0083]	0.60
	${}^{(2_x)}\mathrm{p}_4$: [0.5541 −0.0586 0.0079 0.0022 −0.0086 0.0033 $-3.5354e-04$ $8.5121e-05$]	1.20
5	${}^{(1_x)}\mathrm{p}_5$: [0.4889 −0.1077 −0.0166 −0.0065 0.0605 −0.0093 −0.0872 0.0496]	0.60
	${}^{(2_x)}\mathrm{p}_5$: [0.4889 −0.0582 −0.0072 0.0030 0.0073 −0.0015 −0.0019 $5.5451e-04$]	1.10
6	${}^{(1_x)}\mathrm{p}_6$: [0.4236 −0.1126 −0.0035 −0.0411 −0.2716 0.9252 −1.4262 0.9456]	0.50
	${}^{(2_x)}\mathrm{p}_6$: [0.4236 −0.0465 0.0100 −0.0088 −0.0257 0.0311 −0.0190 0.0055]	1.15
7	${}^{(1_x)}\mathrm{p}_7$: [0.3583 −0.1576 −0.0326 0.2317 −0.7151 2.8838 −4.1411 1.8915]	0.70
	${}^{(2_x)}\mathrm{p}_7$: [0.3583 −0.0830 −0.0180 0.0417 −0.0662 0.1535 −0.1234 0.0313]	1.35
8	${}^{(1_x)}\mathrm{p}_8$: [0.2930 0 0 0 2.4213 −6.3825 6.3295 −2.2830]	0.70
	${}^{(2_x)}\mathrm{p}_8$: [0.2930 0 0 0 0.1844 −0.2543 0.1309 −0.0244]	1.35
9	${}^{(1_x)}\mathrm{p}_9$: [0.3583 0.1624 −0.0356 −0.2598 0.8849 −1.7074 2.0076 −1.0076]	0.50
	${}^{(2_x)}\mathrm{p}_9$: [0.3583 0.0793 −0.0170 −0.0362 0.0619 −0.0479 0.0230 −0.0050]	1.15
10	${}^{(1_x)}\mathrm{p}_{10}$: [0.4236 0.1071 −0.0113 0.0564 −0.0489 −0.0580 0.1083 −0.0455]	0.60
	${}^{(2_x)}\mathrm{p}_{10}$: [0.4236 0.0501 0.0115 0.0066 −0.0107 $-2.2438e-04$ 0.0027 $-6.2319e-04$]	1.10
11	${}^{(1_x)}\mathrm{p}_{11}$: [0.4889 0.1102 −0.0046 −0.0085 0.0375 −0.0364 0.0191 −0.0091]	0.60
	${}^{(2_x)}\mathrm{p}_{11}$: [0.4889 0.0591 −0.0089 −0.0028 0.0100 −0.0038 $3.5664e-04$ $-8.4915e-05$]	1.20
12	${}^{(1_x)}\mathrm{p}_{12}$: [0.5541 0.1102 0.0046 −0.0085 −0.0178 −0.0121 0.0828 −0.0455]	0.60
	${}^{(2_x)}\mathrm{p}_{12}$: [0.5541 0.0591 0.0089 −0.0028 −0.0084 0.0019 0.0021 $-6.2319e-04$]	1.10
13	${}^{(1_x)}\mathrm{p}_{13}$: [0.6194 0.1071 0.0113 0.0564 0.2633 −0.9744 1.5189 −1.0076]	0.50
	${}^{(2_x)}\mathrm{p}_{13}$: [0.6194 0.0501 −0.0115 0.0066 0.0251 −0.0290 0.0175 −0.0050]	1.15
14	${}^{(1_x)}\mathrm{p}_{14}$: [0.6847 0.1624 0.0356 −0.2598 0.8034 −3.2909 4.8573 −2.2830]	0.70
	${}^{(2_x)}\mathrm{p}_{14}$: [0.6847 0.0793 0.0170 −0.0362 0.0569 −0.1290 0.1000 −0.0244]	1.35

The coordinates of the linear trajectories remain constant in the y direction with minimal variation, so the polynomial coefficients of each segment tend toward 0 and are not reflected in the table. ${}^{(j_x)}\mathrm{p}_i$ represents the polynomial coefficient in the x-direction of the i-th segment of the j-th trajectory.

A comparison reveals that the optimized trajectories' joint velocities, accelerations, and jerks are generally of a lower magnitude than those of a randomly generated trajectory. It is noted that all the maximum magnitudes of the joint velocity, acceleration, and jerk profiles of the optimized trajectory are smaller than the random ones, which implies that the optimized trajectory ensures a higher kinematic performance of the robot's rehabilitation training. This implies that the optimized one better conforms to the kinematic characteristics of traditional rehabilitation therapies, where a physician manually drags the affected limbs. The optimized trajectories ensure lighter impacts and a smoother path, thereby guaranteeing the robot with higher motional performance in rehabilitation.

Additionally, as shown in Figure 18a,b, a comparison of the two rehabilitation trajectories reveals that trajectory 1 completes one training cycle within 16.8 s, with the knee joint reaching its maximum flexion at the 8.4-th second, and all ranges of motion meet the set joint rehabilitative criteria. Trajectory 2 completes two training cycles within 16.8 s, with the

hip joint reaching its maximum flexion at the 4.2-th second and at the 12.6-th second, with all movement ranges also meeting the set joint rehabilitative criteria. Moreover, the joint velocity and acceleration curves are smooth and continuously differentiable, and the joint jerk is restricted to zero at the start point, end point, and the point of the maximum flexion, effectively replicating the rehabilitation patterns that occur during traditional rehabilitation therapy, where a physician drags the affected limb. This approach maximizes the safety of the patient's rehabilitation training and simulates the reliable technique of the physician.

As shown in Figure 18g,h, the maximum hip joint jerk of the random trajectory 1 is 10.2 rad/s^3, and the maximum knee joint impact is 24.9 rad/s^3. The maximum jerk on the hip joint of optimized trajectory 1 is 9.3 rad/s^3, and the maximum jerk on the knee joint is 21.3 rad/s^3. The maximum jerk on the hip joint of random trajectory 2 is 2.9 rad/s^3, and the maximum jerk on the knee joint is approximately 5.8 rad/s^3. The maximum jerk on the hip joint of trajectory 1 after optimization is 2.5 rad/s^3, and the maximum jerk on the knee joint is 5.5 rad/s^3. Therefore, the maximum joint jerk of optimized trajectories 1 and 2 is smaller than that of the random trajectories. It is vital in rehabilitation because the maximum jerk is the most likely to cause secondary damage, and the optimized trajectory effectively reduces the maximum jerk during training. In addition, the joint jerk at each moment of the optimized trajectory is almost always smaller than that of the random trajectory, indicating that patients can feel smaller impacts during the overall rehabilitative process, which helps with the comfort of rehabilitation. In summary, the optimized trajectory can effectively improve the safety and comfort of patients' lower-limb joint rehabilitation compared to the random trajectory.

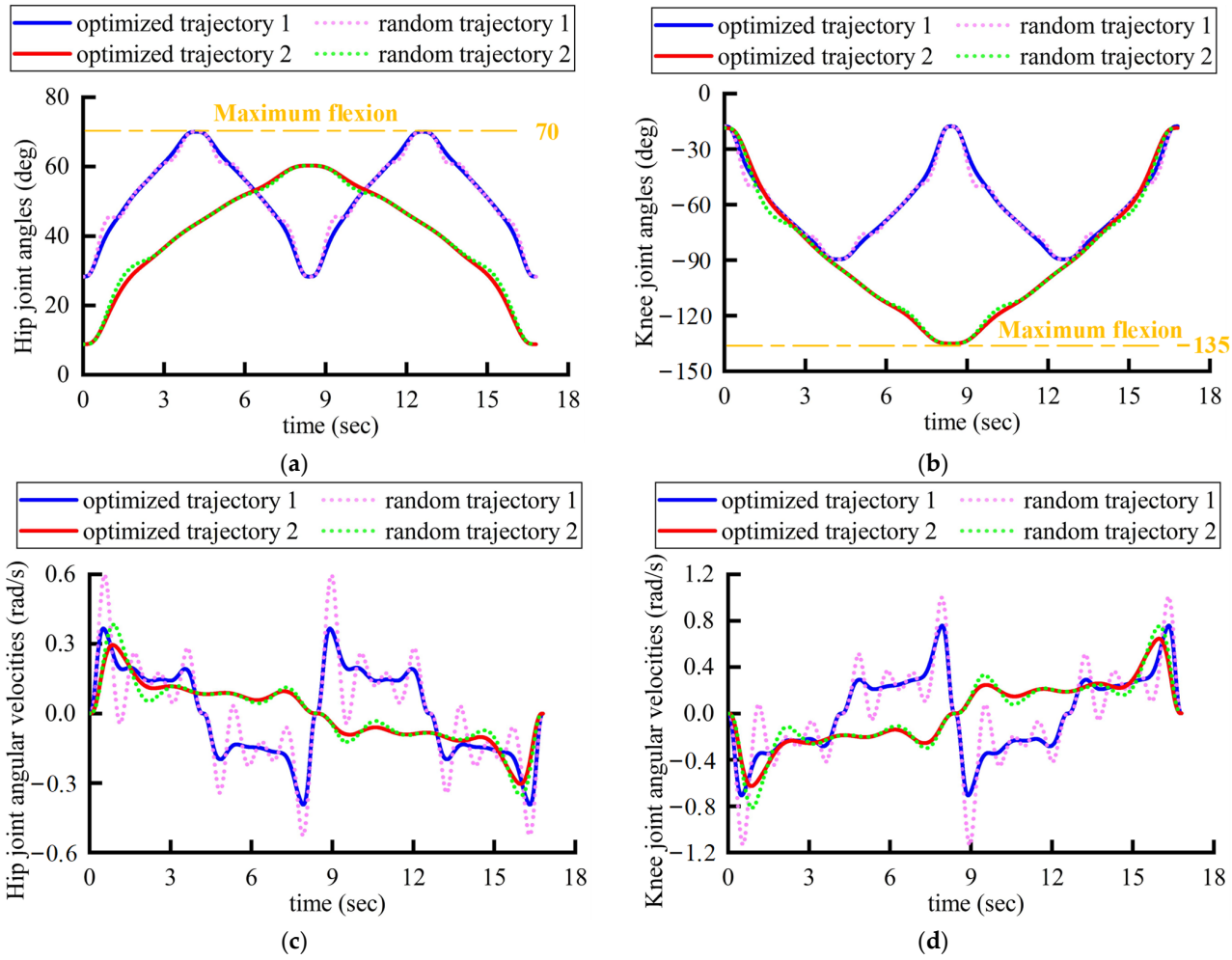

Figure 18. *Cont.*

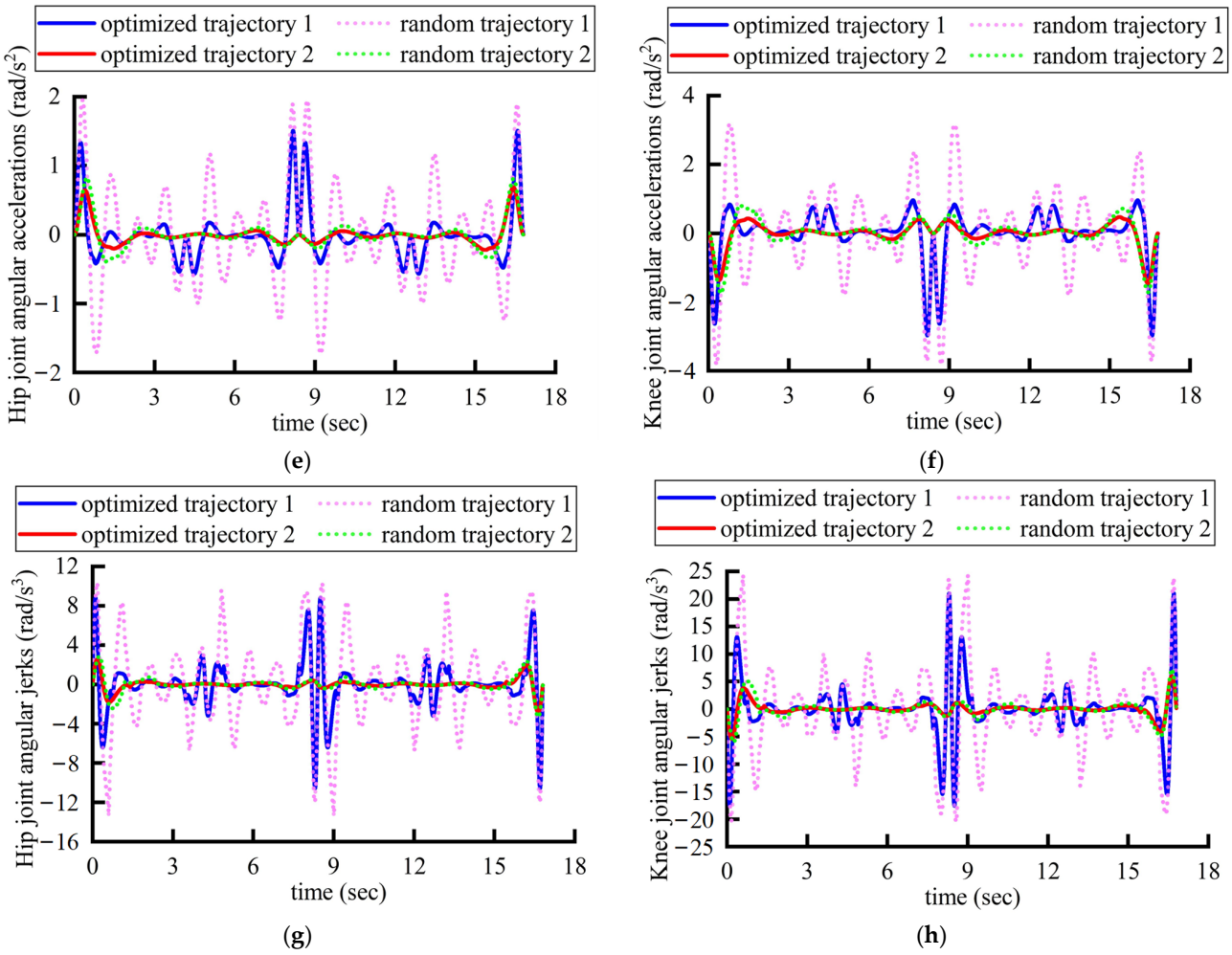

Figure 18. The motion data of the robot's joints for the optimized trajectories and random trajectories: (**a**) displacements of hip; (**b**) displacements of knee; (**c**) velocities of hip; (**d**) velocities of knee; (**e**) accelerations of hip; (**f**) accelerations of knee; (**g**) jerks of hip; (**h**) jerks of knee.

5. Conclusions

This paper introduces a novel linear rehabilitative motion planning approach and successfully demonstrates its integration with a three-degrees-of-freedom (DOF) multi-posture lower-limb rehabilitation robot. Addressing the challenge of incorporating the nuanced treatment expertise of physicians into robotic rehabilitation, we have analyzed the interplay between joint rehabilitation indicators and linear rehabilitation trajectories across diverse action spaces. Subsequently, we designed a joint rehabilitation indicator-based path generation system to enhance the efficiency of rehabilitation path planning for clinicians using the lower-limb rehabilitation robot. To ensure the continuity and minimize the jerks of rehabilitation trajectories, we employed high-order polynomial curves in the trajectory planning process. This approach was further refined through the resolution of a constrained quadratic optimization problem, effectively reducing the jerk of the end effector and the joints of the robot.

Through comparative studies involving Cartesian trajectories determined at equivalent key points, the results revealed that trajectory optimization is indeed feasible for real-time trajectory planning, as evidenced by the low computation times (not exceeding 10 ms). The optimization of trajectories using polynomial curves was found to significantly outperform random trajectories in enhancing the robot's rehabilitative training performance, thereby validating the efficacy of our method within the rehabilitation technology. Furthermore, a comparison of two sets of optimized rehabilitation trajectories, one before and one after the

application of our method, confirmed that the robot's performance was notably improved. Specifically, trajectory 1 and trajectory 2 were tailored to meet the physician's requirements for hip joint extreme flexion and knee joint extreme flexion, respectively. Additionally, both optimized trajectories adhered to other predefined joint rehabilitation indicators, substantiating the effectiveness of our joint rehabilitation indicator-based path generation system in assisting physicians in the operation of rehabilitation robots.

Author Contributions: Conceptualization, X.W., H.W. and B.C.; methodology, X.W. and J.N.; software, X.W. and M.L.; validation, Y.F., J.N. and M.L.; formal analysis, L.S. and B.C.; investigation, X.W.; resources, J.N. and B.C.; data curation, X.W.; writing—original draft preparation, X.W.; writing—review and editing, J.N., H.Y. and M.L.; visualization, X.W.; supervision, Y.F. and L.S.; project administration, H.W., J.N., Y.F., H.Y., M.L. and L.S.; funding acquisition, H.W., J.N., Y.F., H.Y., M.L. and L.S. All authors have read and agreed to the published version of the manuscript.

Funding: This research was funded by the National Key Science and Technology Project Undertaken by Shenzhen, grant number CJGJZD20220517142405013; the Hebei Province Higher Education Humanities and Social Sciences Research Project (Youth Fund Project), grant number SQ2024162; the Ningbo International Cooperation project, grant number 2023H014; the S&T Program of Qinhuangdao, grant number 202401A049; and the Zhejiang Provincial Natural Science Foundation of China, grant number LGF22E050001.

Institutional Review Board Statement: Not applicable.

Informed Consent Statement: Informed consent was obtained from all subjects involved in the study.

Data Availability Statement: Data are contained within the article.

Conflicts of Interest: The authors declare no conflicts of interest.

References

1. Wang, W.; Li, K.; Yue, S.; Yin, C.; Yin, C.; Wei, N. Associations between lower-limb muscle activation and knee flexion in post-stroke individuals: A study on the stance-to-swing phases of gait. *PLoS ONE* **2017**, *12*, e0183865. [CrossRef] [PubMed]
2. Celestino, M.L.; van Emmerik, R.; Barela, J.A.; Bacca, O.; Barela, A.M.F. Effects of limited knee flexion movement in intra-limb gait coordination. *J. Biomech.* **2021**, *128*, 110712. [CrossRef] [PubMed]
3. Li, S. Stiff knee gait disorders as neuromechanical consequences of spastic hemiplegia in chronic stroke. *Toxins* **2023**, *15*, 204. [CrossRef]
4. Rybar, M.M.; Walker, E.R.; Kuhnen, H.R.; Ouellette, D.R.; Berrios, R.; Hunter, S.K.; Hyngstrom, A.S. The stroke-related effects of hip flexion fatigue on over ground walking. *Gait Posture* **2014**, *39*, 1103–1108. [CrossRef]
5. Carda, S.; Invernizzi, M.; Cognolato, G.; Piccoli, E.; Baricich, A.; Cisari, C. Efficacy of a hip flexion assist orthosis in adults with hemiparesis after stroke. *Phys. Ther. Rehabil. J.* **2012**, *92*, 734–739. [CrossRef]
6. Hyngstrom, A.S.; Kuhnen, H.R.; Kirking, K.M.; Hunter, S.K. Functional implications of impaired control of submaximal hip flexion following stroke. *Muscle Nerve* **2014**, *49*, 225–232. [CrossRef]
7. Salzmann, C.; Sehle, A.; Liepert, J. Using the flexor reflex in a chronic stroke patient for gait improvement: A case report. *Front. Neurol.* **2021**, *12*, 691214. [CrossRef]
8. Nadeau, S.; Gravel, D.; Arsenault, A.B.; Bourbonnais, D. Plantarflexor weakness as a limiting factor of gait speed in stroke subjects and the compensating role of hip flexors. *Clin. Biomech.* **1999**, *14*, 125–135. [CrossRef]
9. Schindler-Ivens, S.; Desimone, D.; Grubich, S.; Kelley, C.; Sanghvi, N.; Brown, D.A. Lower extremity passive range of motion in community-ambulating stroke survivors. *J. Neurol. Phys. Ther.* **2008**, *32*, 21–31. [CrossRef]
10. Pollock, C.L.; Hunt, M.A.; Garland, S.J.; Ivanova, T.D.; Wakeling, J.M. Relationships between stepping-reaction movement patterns and clinical measures of balance, motor impairment, and step characteristics after stroke. *Phys. Ther. Rehabil. J.* **2021**, *101*, pzab069. [CrossRef]
11. Gomez-Cuaresma, L.; Lucena-Anton, D.; Gonzalez-Medina, G.; Martin-Vega, F.J.; Galan-Mercant, A.; Luque-Moreno, C. Effectiveness of stretching in post-stroke spasticity and range of motion: Systematic review and meta-analysis. *J. Pers. Med.* **2021**, *11*, 1074. [CrossRef] [PubMed]
12. Bouri, M.; Le Gall, B.; Clavel, R. A new concept of parallel robot for rehabilitation and fitness: The lambda. In Proceedings of the IEEE International Conference on Robotics and Biomimetics (ROBIO), Guilin, China, 19–23 December 2009; pp. 2503–2508. [CrossRef]
13. Simon, A.M.; Kelly, B.M.; Ferris, D.P. Preliminary trial of symmetry-based resistance in individuals with post-stroke hemiparesis. In Proceedings of the 31st Annual International Conference of the IEEE EMBS, Minneapolis, MN, USA, 2–6 September 2009; pp. 5294–5299. [CrossRef]

14. Ho, H.J.; Chen, T.C. Motorized CPM/CAM physiotherapy device with sliding-mode fuzzy neural network control loop. *Comput. Meth. Programs Biomed.* **2009**, *96*, 96–107. [CrossRef] [PubMed]
15. Sun, H.; Zhang, L.; Hu, X.; Tian, L. Experiment study of fuzzy impedance control on horizontal lower limbs rehabilitation robot. In Proceedings of the International Conference on Electronics, Communications and Control (ICECC), Ningbo, China, 9–11 September 2011; pp. 2640–2643.
16. Deaconescu, T.; Deaconescu, A. Pneumatic muscle actuated isokinetic equipment for the rehabilitation of patients with disabilities of the bearing joints. In Proceedings of the International Multi-Conference of Engineers and Computer Scientists (IMECS), Hong Kong, 18–20 March 2009; pp. 1823–1827.
17. Metrailler, P.; Blanchard, V.; Perrin, I.; Brodard, R.; Frischknecht, R.; Schmitt, C.; Fournier, J.; Bouri, M.; Clavel, R. Improvement of rehabilitation possibilities with the MotionMaker (TM). In Proceedings of the 2006 1st IEEE RAS-EMBS International Conference on Biomedical Robotics and Biomechatronics, Pisa, Italy, 20–22 February 2006; pp. 626–631.
18. Schmitt, C.; Métrailler, P.; Al-Khodairy, A.; Brodard, R.; Fournier, J.; Bouri, M.; Clavel, R. The Motion Maker™: A rehabilitation system combining an orthosis with closed-loop electrical muscle stimulation. In Proceedings of the 8th Vienna International Workshop on Functional Electrical Stimulation, Vienna, Austria, 6–9 September 2004; pp. 117–120. [CrossRef]
19. Akdoan, E.; Adli, M.A. The design and control of a therapeutic exercise robot for lower limb rehabilitation: Physiotherabot. *Mechatronics* **2011**, *21*, 509–522. [CrossRef]
20. Hidenori, T. Development of portable therapeutic exercise machine temlx2 influences of passive motion for lower extremities on regional cerebral blood volume. In Proceedings of the Symposium on Biological and Physiological Engineering, Taipei, Taiwan, 7–8 December 2006; pp. 29–31.
21. Bradley, D.; Acosta-Marquez, C.; Hawley, M.; Brownsell, S.; Enderby, P.; Mawson, S. Nexos: The design, development and evaluation of a rehabilitation system for the lower limbs. *Mechatronics* **2009**, *19*, 247–257. [CrossRef]
22. Wang, H.; Feng, Y.; Yu, H.; Wang, Z.; Victor, V.; Du, Y. Mechanical design and trajectory planning of a lower limb rehabilitation robot with a variable workspace. *Int. J. Adv. Robot. Syst.* **2018**, *15*, 1729881418776855. [CrossRef]
23. Hwang, S.H.; Sun, D.I.; Han, J.; Kim, W.S. Gait pattern generation algorithm for lower-extremity rehabilitation–exoskeleton robot considering wearer's condition. *Intell. Serv. Robot.* **2021**, *14*, 345–355. [CrossRef]
24. Long, Y.; Du, Z.J.; Wang, W.D.; Dong, W. Human motion intent learning based motion assistance control for a wearable exoskeleton. *Robot. Comput.-Integr. Manuf.* **2018**, *49*, 317–327. [CrossRef]
25. Hassan, M.; Kadone, H.; Suzuki, K.; Sankai, Y. Wearable gait measurement system with an instrumented cane for exoskeleton control. *Sensors* **2014**, *14*, 1705–1722. [CrossRef]
26. Yoshikawa, K.; Mizukami, M.; Kawamoto, H.; Sano, A.; Koseki, K.; Sano, K.; Asakawa, Y.; Kohno, Y.; Nakai, K.; Gosho, M.; et al. Gait training with hybrid assistive limb enhances the gait functions in subacute stroke patients: A pilot study. *NeuroRehabilitation* **2017**, *40*, 87–97. [CrossRef]
27. Mileti, I.; Taborri, J.; Torricelli, D.; Rossi, S.; Patane, F. Artificial neural network for the identification of postural instability in subject wearing lower limb exoskeleton. In Proceedings of the IEEE International Conference on Metrology for Extended Reality, Artificial Intelligence and Neural Engineering (IEEE MetroXRAINE), Rome, Italy, 26–28 October 2022; pp. 651–655. [CrossRef]
28. Gil-Agudo, A.; Del Ama-Espinosa, A.J.; Lozano-Berrio, V.; Fernández-López, A.; Megía, G.-C.A.; Benito-Penalva, J.; Pons, J.L. Robot therapy with the H2 exoskeleton for gait rehabilitation in patients with incomplete spinal cord injry. A clinical experience. *Rehabilitacion* **2020**, *54*, 54–87. [CrossRef]
29. Patton, J.; Brown, D.A.; Peshkin, M.; Santos-Munné, J.J.; Makhlin, A.; Lewis, E.; Colgate, E.J.; Schwandt, D. KineAssist: Design and development of a robotic overground gait and balance therapy device. *Top. Stroke Rehabil.* **2008**, *15*, 131–139. [CrossRef] [PubMed]
30. Riener, R.; Lünenburger, L.; Jezernik, S.; Anderschitz, M.; Colombo, G.; Dietz, V. Patient-cooperative strategies for robot-aided treadmill training: First experimental results. *J. NeuroEng. Rehabil.* **2005**, *7*, 43. [CrossRef] [PubMed]
31. Duschau-Wicke, A.; von Zitzewitz, J.; Caprez, A.; Lunenburger, L.; Riener, R. Path control: A method for patient-cooperative robot-aided gait rehabilitation. *IEEE Trans. Neural Syst. Rehabil. Eng.* **2010**, *18*, 38–48. [CrossRef] [PubMed]
32. van Kammen, K.; Boonstra, A.M.; van der Woude, L.H.V.; Reinders-Messelink, H.A.; den Otter, R. The combined effects of guidance force, bodyweight support and gait speed on muscle activity during able-bodied walking in the Lokomat. *Clin. Biomech.* **2016**, *36*, 65–73. [CrossRef]
33. Veneman, J.F.; Kruidhof, R.; Hekman, E.E.G.; Ekkelenkamp, R.; Van Asseldonk, E.H.F.; van der Kooij, H. Design and evaluation of the LOPES exoskeleton robot for interactive gait rehabilitation. *IEEE Trans. Neural Syst. Rehabil. Eng.* **2007**, *15*, 379–386. [CrossRef]
34. Banala, S.K.; Agrawal, S.K.; Scholz, J.P. Active Leg Exoskeleton (ALEX) for Gait Rehabilitation of Motor-Impaired Patients. In Proceedings of the IEEE 10th International Conference on Rehabilitation Robotics, Noordwijk, The Netherlands, 13–15 June 2007; p. 401. [CrossRef]
35. Guo, B.; Han, J.; Li, X.; Wu, P.; Zhang, Y.; You, A. A wearable somatosensory teaching device with adjustable operating force for gait rehabilitation training robot. *Adv. Mech. Eng.* **2017**, *9*, 6293. [CrossRef]
36. Guo, B.; Han, J.; Li, X.; Fang, T.; You, A. Research and design of a new horizontal lower limb rehabilitation training robot. *Int. J. Adv. Robot. Syst.* **2016**, *13*, 62032. [CrossRef]
37. Lu, Y.; Wang, H.; Niu, J.; Lu, Z.; Liu, C.; Feng, N. Jump motion intention recognition and brain activity analysis based on EEG signals and Vision Transformer model. *Biomed. Signal Process. Control* **2025**, *100*, 107001. [CrossRef]

38. Mercorelli, P. Using Fuzzy PD Controllers for Soft Motions in a Car-like Robot. *Adv. Sci. Technol.-Res.* **2018**, *3*, 380–390. [CrossRef]
39. Kruse, O.; Mukhamejanova, A.; Mercorelli, P. Super-Twisting Sliding Mode Control for Differential Steering Systems in Vehicular Yaw Tracking Motion. *Electronics* **2022**, *11*, 1330. [CrossRef]
40. Wang, X.; Wang, H.; Zhang, B.; Zheng, D.; Yu, H.; Cheng, B.; Niu, J. A Multistage Hemiplegic Lower-Limb Rehabilitation Robot: Design and Gait Trajectory Planning. *Sensors* **2024**, *24*, 2310. [CrossRef]
41. Wu, G.L.; Zhang, S.D. Real-time jerk-minimization trajectory planning of robotic arm based on polynomial curve optimization. *Proc. Inst. Mech. Eng. Part C-J. Eng. Mech. Eng. Sci.* **2022**, *236*, 10852–10864. [CrossRef]

Disclaimer/Publisher's Note: The statements, opinions and data contained in all publications are solely those of the individual author(s) and contributor(s) and not of MDPI and/or the editor(s). MDPI and/or the editor(s) disclaim responsibility for any injury to people or property resulting from any ideas, methods, instructions or products referred to in the content.